COMPRESSED SENSING TECHNIQUES FOR ACCELERATED MAGNETIC RESONANCE IMAGING

A THESIS SUBMITTED TO
THE GRADUATE SCHOOL OF ENGINEERING AND SCIENCE
OF BILKENT UNIVERSITY
IN PARTIAL FULFILLMENT OF THE REQUIREMENTS FOR
THE DEGREE OF
MASTER OF SCIENCE
IN
ELECTRICAL AND ELECTRONICS ENGINEERING

By
Efe Ilıcak
July 2017

Compressed sensing techniques for accelerated magnetic resonance imaging
By Efe Ilıcak
July 2017

We certify that we have read this thesis and that in our opinion it is fully adequate, in scope and in quality, as a thesis for the degree of Master of Science.

Tolga Çukur(Advisor)

Emine Ülkü Sarıtaş Çukur

Behçet Murat Eyüboğlu

Approved for the Graduate School of Engineering and Science:

Ezhan Karaşan
Director of the Graduate School

ABSTRACT

COMPRESSED SENSING TECHNIQUES FOR ACCELERATED MAGNETIC RESONANCE IMAGING

Efe Ilıcak
M.S. in Electrical and Electronics Engineering
Advisor: Tolga Çukur
July 2017

Magnetic resonance imaging has seen a growing interest in the recent years due to its non-invasive and non-ionizing nature. However, imaging speed remains a major concern. Recently, compressed sensing theory has opened new doors for accelerated imaging applications. This dissertation studies compressed sensing based reconstruction strategies for accelerated magnetic resonance imaging, specifically for angiography and multiple-acquisition methods. For magnetic resonance angiography, we propose a novel approach that improves scan time efficiency while suppressing background signals. In this study, we attain high-contrast angiograms from undersampled data by utilizing a two-stage reconstruction strategy. Simulations and in vivo experiments demonstrate that the developed strategy is able to relax trade-offs between image contrast and scan efficiency without compromising vessel depiction. For multiple-acquisition balanced steady state free precession imaging, we develop a framework that jointly reconstructs undersampled phase-cycled images. This approach is able to improve banding artifact suppression while maintaining scan efficiency. Results show that the proposed method is able to attain high-quality reconstructions even at high acceleration factors.

Overall, the findings presented in this thesis indicate that compressed sensing reconstructions represent a promising future for rapid magnetic resonance imaging. Consequently, compressed sensing reconstruction techniques hold a great potential to change the time-consuming clinical imaging practices.

Keywords: Compressed sensing, magnetic resonance imaging, rapid imaging.

ÖZET

HIZLANDIRILMIŞ MANYETİK REZONANS GÖRÜNTÜLEME İÇİN SIKIŞTIRILMIŞ ALGILAMA TEKNİKLERİ

Efe Ilıcak
Elektrik ve Elektronik Mühendisliği, Yüksek Lisans
Tez Danışmanı: Tolga Çukur
Temmuz 2017

Manyetik rezonans görüntüleme, invazif ve iyonlaştırıcı olmamasından dolayı son yıllarda artan bir ilgi görmektedir. Ancak görüntüleme hızı, temel bir problem teşkil etmektedir. Yakın zamanda sıkıştırılmış algılama kuramı, hızlandırılmış görüntüleme uygulamaları için yeni fırsatlar oluşturmuştur. Bu tez, özellikle anjiyografi ve çoklu çekim yöntemlerinde kullanılmak üzere geliştirilmiş, sıkıştırılmış algılama kuramına dayalı geriçatım tekniklerini incelemektedir. Manyetik rezonans anjiyografi için, görüntü süresi verimliliğini artırırken arkaplan sinyallerini baskılayan yeni bir yöntem önerilmiştir. Bu çalışmada yüksek kontrastlı anjiyogramlar, eksik örneklendirilmiş veriden iki aşamalı bir geriçatım tekniği ile elde edilmektedir. Geliştirilen yöntemin görüntü kontrastı ile görüntüleme verimliliği arasındaki dengeyi, damar görselliğini bozmadan gevşetebildiği, simusayon ve in vivo deneyler ile gösterilmiştir. Çoklu çekim dengeli kararlı-durum serbest devinim görüntüleme teknikleri için ise, eksik örneklendirilmiş faz döngülü görüntüleri birlikte işleyen bir geriçatım tekniği geliştirilmiştir. Bu yöntem görüntüleme verimliliğini korurken, bükülme artifaktlarının baskılanmasını iyileştirebilmektedir. Elde edilen sonuçlar, bu yöntemin yüksek hızlandırma değerlerinde bile yüksek kaliteli geriçatımlar elde edebildiğini göstermektedir.

Sonuç olarak bu tezdeki bulgular, sıkıştırılmış algılamaya bağlı geriçatım yöntemlerinin, hızlı manyetik rezonans görüntüleme için umut vadeden bir gelişme olduğunu göstermektedir. Buna bağlı olarak sıkıştırılmış algılama geriçatma tekniklerinin, zaman alıcı klinik görüntüleme uygulamalarını değiştirmek için büyük bir fırsat sunduğunu görülmektedir.

Anahtar sözcükler: Sıkıştırılmış algılama, manyetik rezonans görüntüleme, hızlı

görüntüleme.

Acknowledgement

First of all, I would like to express my sincere gratitude to Prof. Tolga Çukur, who has supported me with his endless guidance. This thesis would not been possible without his wisdom and his confidence in me. He has given me the tools as well as the freedom to pursue my research interests.

I would like to extend my thanks to Prof. Sarıtaş. Her precious insights and her unparalleled teaching skill have taught me what I know about MRI and many imaging modalities.

I would also like to thank Prof. Atalar for founding UMRAM and providing this amazing environment. With his vision, we are able embark on academic endeavors and be at the forefront of scientific discovery.

During my time at UMRAM and ICON Lab, I was lucky enough to know and work with many great people. In particular, I am grateful to Ümit Keleş, Özgür Yılmaz, Toygan Kılıç, Salman Dar for helping me throughout this journey and Erdem Bıyık for being the perfect intern. I would also like to thank Aydan Ercingöz for creating order from chaos and keeping UMRAM functioning; Umut Gündoğdu and Mustafa Can Delikanlı for teaching me how to use MRI scanner and helping me with my never-ending questions.

I also owe special thanks to my brother from another mother, Uras Demir; and my dear friends, Canberk Pay, Goksü Yamaç, Emir Artık, and Sezer Yılmazer for all the help and motivation they provided me to write this thesis.

Last but not the least, I would like to thank my family, my mother Meltem, my father Sinan and my brother Ege, for their endless love and unconditional support. Words cannot describe how grateful I am. Without them, none of this would be possible.

Contents

List of Figures

List of Tables

Chapter 1

Introduction

Magnetic resonance imaging (MRI) is a noninvasive imaging modality that does not require the use of ionizing radiation. Thanks to its safety and unparalleled soft tissue contrast properties, it has gained widespread usage in the clinical settings [1, 2]. However, the incorporation of MRI techniques into clinical practice has been hindered due to its relatively long examination times compared to other imaging modalities such as computed tomography or ultrasound imaging [2, 3]; where this limitation arises from both physical and physiological constraints [4]. Over the last decades, many successful approaches have been proposed to improve the scan efficiency, such as the development of fast switching magnetic field gradients; implementation of rapid imaging sequences(e.g., gradient-echo, fast-spin echo, or steady-state free precession sequences); development of multiple coil receiver arrays and parallel imaging techniques, and more recently by using sparsity based compressed sensing applications [5, 3, 6, 4].

Originally emerged from information theory, compressed sensing aims to reconstruct signals from relatively small number of samples compared to traditionally required [7]. This is partly possible due to the compressibility of the underlying signal in a known transform domain. Successful application of compressed sensing can be summarized in three requirements: (a) The sampled signal should be sparse or compressible in a known transform domain (e.g., wavelet domain), (b)

the sampling should create incoherent aliasing artifacts in the compression transform domain, (c) a nonlinear reconstruction algorithm should be used to enforce sparsity and data consistency. When these three requirements are met, signals can be recovered from significantly lower number of samples [4, 8, 9]. For MRI, these conditions can be matched since MR images are known to be compressible, incoherence can be achieved through random undersampling in k-space, and finally there are efficient algorithms for nonlinear reconstructions [7]. With MRI being a natural fit and its potential to reduce scan time constraints, compressed sensing has sparked a great interest in the MRI community with applications including, but not limited to, anatomical imaging and angiography [4, 8].

Magnetic imaging methods that provide the visualization of blood vessels are referred as magnetic resonance angiography (MRA) methods. These methods can be categorized into two main groups, contrast-enhanced (CE-MRA) and non-contrast-enhanced (NCE-MRA), with the prior utilizing intravenous injection of contrast agents to visualize blood vessels and the later utilizing the intrinsic properties of blood tissue. In the case of non-contrast-enhanced angiography (NCE-MRA), time-of-flight and phase contrast methods rely on the motion of the blood and steady-state method relies on the magnetic properties of blood to generate contrast between vasculature and tissue [10]. Contrast-enhanced MRA methods have gained popularity due to their ease of use, and their ability to quickly produce high-quality diagnostic images of large vascular territories. Currently, Gadolinium-based contrast agents (GBCA) are the most commonly used contrast materials. Since their approval in the 1980s, they have been an important tool for lesion detection and characterization [11]. Similar to computed tomography angiography, CE-MRA provides reliable enhancement of the arterial lumen during the arterial phase of the Gadolinium bolus injection, and can rival digital subtraction angiography in image quality and diagnostic accuracy [12]. However, the bolus timing requirements limit the temporal resolution, spatial resolution, signal-to-noise ratio; the addition of contrast agent increases the already expensive scan cost; and recent studies identified a connection between the GBCAs and a fatal condition called nephrogenic systemic fibrosis in patients with advanced renal diseases [13, 14, 15, 11]. Besides the financial and safety

benefits, the NCE-MRA examinations can be repeated in case of patient motion or technical errors, and can serve as backup examinations before the injection of contrast agents [15].

As a consequence, the advantages has spurred a renewed interest in the NCE-MRA methods [14]. This resurgence of interest ranges from imaging the renal arteries in the abdomen to cerebral arteries, from thoracic aorta to distal vessels [13, 16, 17, 18, 19]. The NCE-MRA methods can be categorized into two classes: flow-dependent and flow-independent. The early non-contrast techniques such as time-of-flight (TOF) and phase contrast (PC) methods generate the contrast by using the fact that blood is flowing inside stationary tissue. However, these methods suffer from reduced contrast in slow or retrograde flow regions, as seen in the cases with stenosis [19]. In contrast, the flow-independent techniques such as balanced steady-state free precession (bSSFP) depend on the magnetic properties of blood tissue and can generate blood-background contrast even in the cases of slow flow [14, 8]. While these methods have proven their usefulness in offering sensitive assessments of vessel morphology, high spatial resolution is needed for diagnostic quality [20]. Furthermore, given the fact that spatial resolution is directly related to acquisition time, the image quality can be limited by the scan time constraints. Therefore, acceleration strategies that improve scan efficiency can greatly increase the clinical potential of NCE-MRA. As a result, many recent studies have proposed various techniques to accelerate acquisitions, including view-ordering [21], parallel imaging [22, 23, 20], and more recently compressed sensing methods [8, 20, 24, 25].

Another important application of compressed sensing can be found in the usage of bSSFP sequence for anatomical imaging. In recent year, bSSFP sequence has gained popularity as it can provide high signal to noise ratio in short repetition times; and found wide use in numerous MRI applications, such as musculoskeletal imaging, interventional imaging [26, 27, 28, 29, 30, 31]. However, the bSSFP signal depends on the local resonant frequency and magnetization profile, which yields increased sensitivity to magnetic field inhomogeneities. Therefore, bSSFP sequence suffers from irrecoverable signal losses, called banding artifacts, in regions with large off-resonant frequencies [29, 31, 32]. A common approach to

mitigate the banding artifacts is to use multiple-acquisition bSSFP technique [33, 32]. In this method, spatially non-overlapping banding artifacts are created by acquiring the images by either changing the center frequency directly or by altering the radio frequency pulse between repetition times. Afterwards, the phase-cycled images can be combined to obtain artifact free image. Unfortunately, the speed advantage of this sequence is diminished due to the prolonged acquisition time with additional acquisitions. Thus, acceleration strategies that improve the scan efficiency are of great interest.

1.1 Outline of the thesis

Chapter 2 focuses on a novel approach that improves scan efficiency while suppressing background signals for accelerated MRA acquisitions. In this work, we attain high-contrast angiograms from undersampled data by utilizing a two-stage reconstruction strategy. In the first step, we generate 3D vessel maps using a tractographic segmentation on Fourier reconstructions of undersampled data. In the second step, targeted reconstructions are performed based on these maps with spatially adaptive ℓ_1-norm and total-variation penalties to dampen background signals while preserving the depiction of vasculature. Simulations and in vivo experiments demonstrates that the developed strategy is able to relax trade-offs between image contrast, resolution and scan efficiency without compromising vessel depiction. Radiological assessments also demonstrate that the proposed method is able to outperform conventional compressed sensing reconstructions.

Chapter 3 introduces a novel approach for multiple-acquisition balanced steady-state free precession imaging. In this framework, acquisitions are accelerated to keep the total scan time equivalent to a single fully-sampled acquisition. Similar to parallel imaging applications, we model each phase-cycled bSSFP image as the product of banding artifact-free image with a respective bSSFP spatial profile and jointly process these images to mitigate banding artifacts. During the reconstructions, missing k-space samples are linearly synthesized from acquired data. To alleviate the aliasing artifacts and noise interference, joint-sparsity and

total-variation penalties are utilized. Simulations and experiments show that the proposed approach is able to achieve high-quality reconstructions with high-spatial-frequency information, even at high acceleration factors.

Finally, Chapter 4 summarizes the contributions of this thesis and discusses possible future research directions.

Chapter 2

Targeted vessel reconstruction for vessel preservation in non-contrast-enhanced angiography

This chapter is based on publication 'Targeted vessel reconstruction in noncontrast-enhanced steady-state free precession angiography', Ilicak, E., Cetin, S., Bulut, E., Oguz, K. K., Saritas, E. U., Unal, G., and Çukur, T., NMR Biomed. 29: 532544, 2016.

List of Abbreviations

CE	Contrast-enhanced
CS	Compressed sensing
CS_{cont}	Conventional CS reconstruction with matched contrast to TCS
CS_{high}	Conventional CS reconstruction with heavier regularization weight
CS_{int}	Intensity-weighted CS reconstruction
CS_{IR}	Iteratively reweighted CS reconstruction
CS_{low}	Conventional CS reconstruction with conservative regularization weight
DI	Dispersion index
FIA	Flow-independent angiography
FWHM	Full-width at half-maximum
MIP	Maximum intensity projection
MRA	Magnetic resonance angiography
NCE	Non-contrast-enhanced
R	Acceleration factor
ROI	Region-of-interest
SNR	Signal-to-noise ratio
SSFP	Steady-state free precession
TCS	Targeted compressed sensing reconstruction
$TCS_{n\ell_1}$	TCS reconstruction with fixed ℓ_1 penalty
TCS_{nTV}	TCS reconstruction with fixed TV penalty
TE	Echo time
TR	Repetition time
TV	Finite differences (total-variation)
Y	Acquired data
ZF	Zero-filled Fourier

2.1 Introduction

Non-contrast-enhanced MR angiography (NCE MRA) offers great potential in monitoring of atherosclerotic diseases, because it prevents complications due to contrast agents leveraged in routine contrast-enhanced (CE) examinations [34]. Various successful approaches have been proposed to acquire NCE angiograms, including time-of-flight angiography, phase-contrast angiography, fresh-blood imaging and flow-independent angiography (FIA) [35]. While these methods offer sensitive assessments of vessel morphology, image quality may be compromised due to limitations on scan time.

In the case of FIA, blood is delineated based on intrinsic $T_{1,2}$ and chemical shift differences among tissues. FIA employs magnetization-prepared, segmented steady-state free precession (SSFP) sequences to generate blood-background contrast [14, 36]. This preparation overhead reduces scan efficiency and limits the achievable contrast and resolution [37], which is a concern for many other NCE methods as well [35]. Note that limited contrast levels due to unwanted interference from background tissues can severely degrade the quality of vessel depiction. Therefore, acceleration strategies that improve scan efficiency while suppressing background signals can greatly increase the clinical potential of NCE MRA.

Due to the inherent structural sparsity of angiograms, acceleration can be achieved through undersampling followed by sparse reconstructions [4, 25, 8, 20, 38]. To suppress aliasing artifacts and noise, penalties are applied typically based on ℓ_1-norm or spatial finite differences of reconstructed images [39, 4, 40, 8]. Relative weighting of penalties with respect to a data consistency term is a critical determinant of image quality in these reconstructions [4]. Small weights can lead to insufficient artifact suppression and elevated background signals, whereas large weights can cause loss of relatively small or low-contrast vessel signals [8]. This results in a fundamental compromise between blood-background contrast and vessel preservation.

Several important approaches have been proposed to enhance angiographic

reconstructions based on prior information [41, 42, 43]. Methods that require high-quality prior acquisitions [41, 42] are not directly applicable to undersampled NCE MRA, where data are readily corrupted by aliasing and noise interference. Other methods exploiting temporal image correlations in dynamic acquisitions [43] may be inadequate for static, high-spatial-resolution FIA targeted here.

Previous studies have also leveraged region-adaptive reconstructions to improve quality of angiograms [44, 45, 46, 47, 48, 49]. A group of studies have employed support detection for vascular masking in CE angiograms [44, 45]. Vascular masking relies on heavily-suppressed static tissue in CE MRA, whereas blood-background contrast can be relatively impaired in NCE MRA. An alternative method is to utilize user-specified regions-of-interest (ROIs) for support detection [46, 47, 48]. However, such manual ROIs can be broad and poorly localized to individual vessels. A recent study further proposes 2D vessel segmentations to apply a spatially-varying ℓ_1-penalty [49]. While this approach is promising, it does not consider the full 3D structure of vessels and finite-differences penalties that may be critical for interference suppression.

Here we propose to attain high-contrast angiograms from undersampled data via a two-stage reconstruction. First, we generate 3D vessel maps using a tractographic segmentation on Fourier reconstructions of undersampled NCE data [50]. To dampen background signals, we then perform targeted reconstructions with spatially-adaptive ℓ_1-norm and total-variation penalties based on these maps. As demonstrated with simulations and in vivo experiments, the proposed strategy yields higher levels of background suppression compared to regular reconstructions, without compromising vessel depiction.

2.2 Methods

In this work, we acquire peripheral angiograms in the extremities using a flow-independent technique and variable-density random sampling across k-space. We first obtain Fourier reconstructions of undersampled data following zero-filling

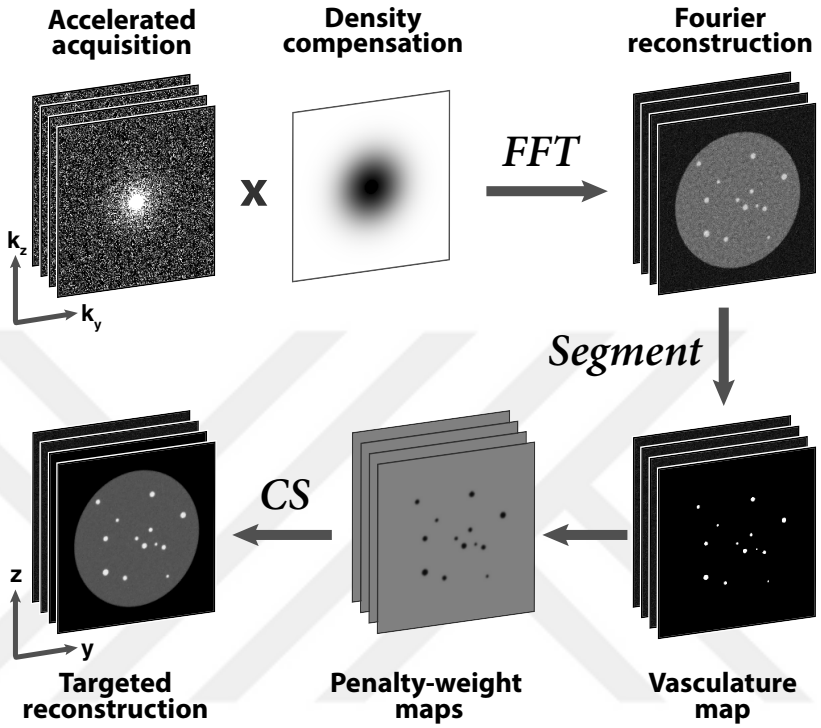

Figure 2.1: Proposed reconstruction strategy. Angiograms with variable-density undersampling in k-space are density-compensated and transformed to obtain Fourier reconstructions (ZF). A segmentation algorithm is then employed to trace vessel trees across the volume. In conventional CS, penalty terms are weighted uniformly across images. Here penalty weights are selected based on segmented vasculature maps: smaller weights at vessel locations enabling targeted reconstructions. Note that data are not density compensated during CS, but only to obtain ZF used for segmentation.

and density compensation in k-space. We then leverage a powerful segmentation algorithm that jointly models tubular sections and branching structures to extract vasculature maps from these initial reconstructions. Finally, we perform targeted reconstructions, where these vasculature maps guide the enforcement of sparsity and total-variation constraints. The workflow of the proposed strategy is illustrated in Fig. 2.1, and individual stages are described in detail in the following sections.

2.2.1 Pulse Sequence

FIA of the peripheral extremities were acquired with a three-dimensional (3D) magnetization-prepared pulse sequence [14, 37]. T_2-prepared magnetization was captured with segmented, centric square-spiral phase-encode ordering [36]. Each segment started with a linearly ramped series of RF excitations to minimize signal oscillations [51]. Afterwards, fat-supressed data were acquired using an alternating repetition time SSFP sequence kernel [14]. A recovery period was inserted between consecutive segments for magnetization recovery.

2.2.2 Sampling Patterns

To accelerate acquisitions, random sampling patterns were generated with a variable sampling density across k-space. Isotropic acceleration in two phase-encode dimensions was generated based on a polynomial density [4, 8, 52],

$$P(k_r) = a_1(1 - k_r)^d + a_2 \tag{2.1}$$

where k_r is the k-space radius, d and $a_{1,2}$ are constants that characterize the polynomial. Full sampling was utilized in the central 2% of k-space. For a given d, candidate sets of $a_{1,2}$ that yield the target acceleration factor (R) were determined using a binary search algorithm. The resulting density for each set was used to generate 1000 random sampling patterns through a Monte Carlo simulation [4]. Only patterns with a total number of samples within 1% of the ideal number (based on R) were accepted. The point spread function (PSF) of each pattern was calculated by taking the inverse Fourier transform of the pattern, and thus assuming an impulse object in the image domain. The level of aliasing energy was then taken as the magnitude-sum of all pixels apart from the origin. The optimal sampling pattern was selected to attain minimal aliasing energy (see Fig. 2.2).

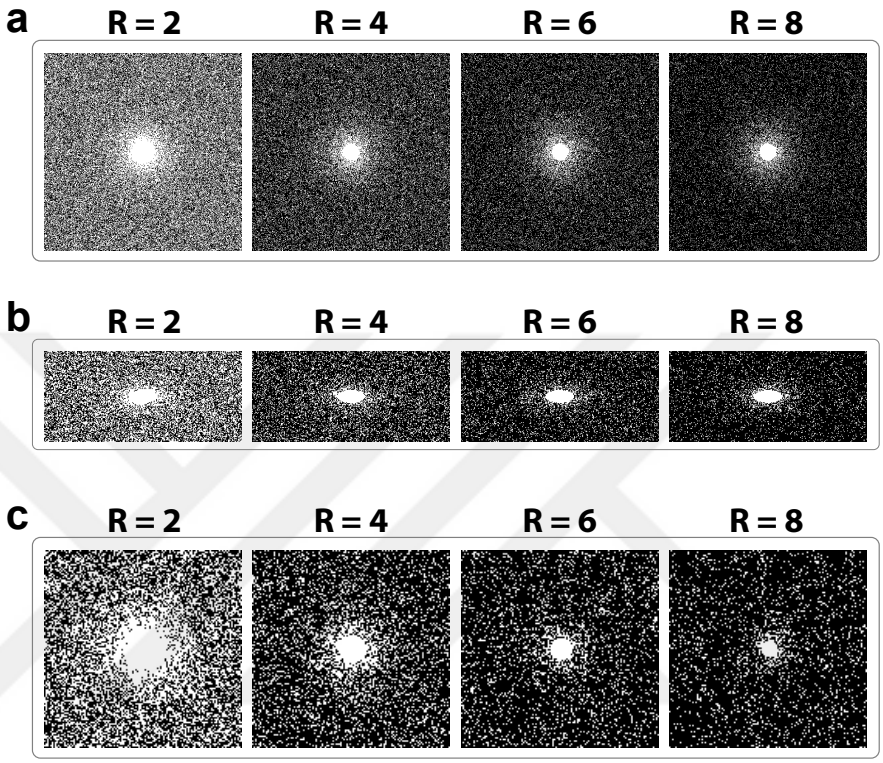

Figure 2.2: Variable-density random sampling masks used at each acceleration factor R=2-8. **(a)** Sampling masks (384×384) for phantom data. **(b)** Sampling masks (240×110) for hand data. **(c)** Sampling masks (128×128) for lower leg and foot data.

2.2.3 Vasculature Mapping

Previous MRA studies have primarily employed vessel segmentations to enhance arterial-venous separation [53, 54] and to extract morphological features such as lumen size [55, 56, 57]. Here we propose to use segmented vessel maps to enhance blood/background contrast in NCE MRA. We leverage a segmentation approach that we have demonstrated thoroughly for synthetic, coronary and cerebral angiograms [58, 59, 50]. Our method jointly models branching structures with tubular sections by leveraging a fourth-order tensor model [59, 50]. The tensor at each voxel in the vessel tree is constructed via non-negative least-squares fitting performed on measurements of image gradient at 64 different orientations. This tensor is then decomposed into its singular vectors to identify major vessel tracts,

including both tubular sections as well as a variety of n-furcations such as Y-, T-, asymmetric- and crossing-junctions [50]. Starting from few seed points, this segmentation method can extract entire vessel trees in the extremities in less than 3 minutes (see Fig. 2.3).

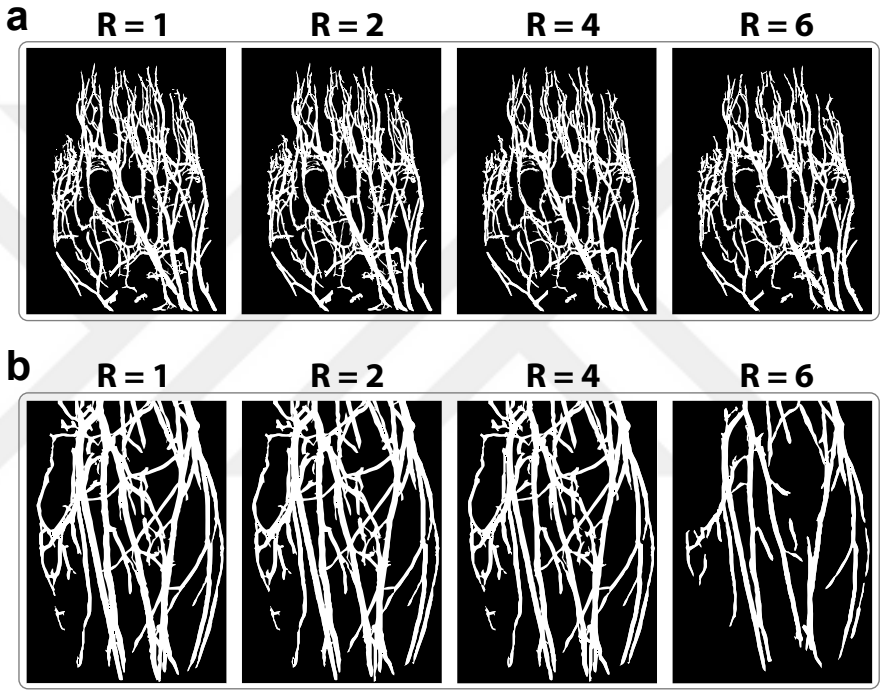

Figure 2.3: Vasculature maps were segmented from undersampled angiograms at acceleration factors R = 1-6. Vessel volumes for hand angiograms **(a)** and lower leg angiograms **(b)** are visualized with maximum-intensity projections (MIPs). Segmentation results at R = 1 (fully-sampled), 2 and 4 are visually similar to each other. For higher R, losses in vessel volume are apparent particularly small vessels. The percentage volume loss in each map is listed with respect to the ideal map at R = 1.

To extract vasculature maps, we first obtained zero-filled reconstructions of undersampled data. Data were compensated for variable k-space sampling density, and zero-padded in three dimensions to double the k-space extent and minimize partial volume effects. To reduce noise levels, reconstructions were smoothed with a Gaussian kernel of width 7 and full-width at half-maximum (FWHM) of 1. Afterwards, manual seed selection was performed to initiate the segmentation procedure. The seed points were selected on tubular sections of major vessels to

avoid vessel junctions. The seeds were placed in vessels of high signal intensity located in superior or inferior cross-sections. The number of seeds prescribed for each anatomy depended on the number of disconnected vessel trees that need to be traced. Seven seeds for hand, five seeds for lower leg and foot angiograms were selected inside major vessel branches. The seed points were identical across R.

2.2.4 Targeted Compressed-Sensing Reconstructions

Compressed-sensing (CS) can estimate missing samples in MRI acquisitions when data have a compressible representation in a linear transform domain, and sampling patterns yield incoherent aliasing in this domain [4]. Nonlinear algorithms are then used during CS reconstructions to enforce compressibility and consistency with the acquired data. MRA datasets contain bright blood vessels surrounded by low-contrast background tissues. Therefore, CS is highly adept at reconstructing heavily undersampled angiograms [8, 39, 40, 25, 20, 38].

2.2.4.1 Optimization framework

Here angiographic reconstructions are obtained via the following optimization [4, 8, 52]:

$$\min_{m} \quad \|F_u m - Y\|_2^2 + \|\lambda_1 \circ m\|_1 + \|\lambda_2 \circ \Delta m\|_1 \tag{2.2}$$

where m is the reconstructed image, and the first term enforces consistency by minimizing the ℓ_2-norm difference between the Fourier transform of the reconstruction ($F_u m$) and the acquired data (Y). Remaining are penalty terms,

$$\|\lambda_1 \circ m\|_1 = \sum_{i,j} \lambda_1(i,j)\,|m(i,j)| \tag{2.3}$$

$$\begin{aligned} \|\lambda_2 \circ \Delta m\|_1 = \sum_{i,j} \lambda_2(i,j)\,\{&|m(i+1,j) - m(i,j)| \\ &+ |m(i,j+1) - m(i,j)|\} \end{aligned} \tag{2.4}$$

where $\circ$ is the Schur product, Δ is the summation of finite-differences transforms across cardinal dimensions, and i, j are the row and column indices of the image

matrix. The ℓ_1-norm penalty enforces sparse reconstructions in the image domain. The finite differences penalty, $TV(m)$ (i.e., total variation), enforces block-wise image homogeneity for denoising.

The problem in Eq. 2.2 was solved using a nonlinear conjugate-gradient algorithm, implemented in MATLAB (Mathworks, Inc.). To compute the conjugate gradient of the ℓ_1-norm, a fixed smoothing parameter of 10^{-15} was added during the absolute value calculation in all iterations. Stopping criteria was an improvement in the objective below a 0.1% threshold, which was observed to yield high quality reconstructions in previous studies [4, 8, 52].

2.2.4.2 Conventional weight selection

In conventional CS, $\lambda_{1,2}$ are uniform scalars across the entire image. Reconstructions were performed across a broad range of penalty weights, similar to previously considered ranges [52, 60]. λ_1 was varied in the range [0 0.800] with a step size of 0.0005 in [0 0.040], and 0.020 in the remaining range. Meanwhile, λ_2 was varied with a step size of 0.0005 in the range [0 0.040]. λ_2 values greater than 0.040 caused undesirably high levels of block artifacts. The smallest pair of weights yielding sufficient artifact/noise suppression, without causing distortions or vessel loss were determined by visual inspection and denoted as $\lambda_{1,2} = \lambda_{1o,2o}$ (see Table 2.1).

2.2.4.3 Targeted weight selection

In angiograms, vessels appear as bright, small ellipsoidal structures in axial cross-sections, whereas background tissues appear as dark, broad regions [52]. Larger λ_1 values promoting background sparsity will cause inadvertent loss of vessel signals. In addition, large λ_2 values promoting effective background denoising can yield suboptimal depiction of small vessels with limited contrast.

Here we propose to utilize spatially-adaptive ℓ_1-norm and TV penalties based

Table 2.1: Reconstruction Parameters

	Phantom			In Vivo	
R	λ_{1o}	λ_{2o}	$\lambda_{1o,cont}$	λ_{1o}	λ_{2o}
1	0.032	0.032	0.520	0.014	0.014
2	0.024	0.024	0.400	0.010	0.010
4	0.016	0.016	0.340	0.006	0.006
6	0.008	0.008	0.240	0.001	0.002
8	0.004	0.004	0.120	0.0005	0.001

Reconstruction parameters for phantom and in vivo data at various acceleration factors (R). $\lambda_1 = 10\lambda_{1o}$ for CS_{high}, $\lambda_1 = \lambda_{1o,cont}$ for CS_{cont}, and $\lambda_1 = \lambda_{1o}$ for all remaining reconstructions. $\lambda_2 = \lambda_{2o}$ for all reconstructions. With this selection, TCS reconstructions scaled the ℓ_1-norm penalty from $10\lambda_{1o}$ in background to λ_{1o} in vessels, and the TV penalty from λ_{2o} in background to $\lambda_{2o}/10$ in vessels.

on a spatial weight map derived from vessel segmentations. The binary segmentations indicate the location of vessels across the imaging volume. To improve robustness against segmentation errors and partial volume effects near the vessel boundaries, segmentations were dilated by one pixel in all dimensions and linearly ramped down from 1 to 0 across the dilated region. The maps were subtracted from 1 and normalized to calculate $W(i,j)$ that decreased from r ($r \geq 1$) to 1. This spatial map was then used to modify the penalty weights as follows:

$$\lambda_1(i,j) \rightarrow \lambda_1 W(i,j) \tag{2.5}$$

$$\lambda_2(i,j) \rightarrow \lambda_2 W(i,j)/r \tag{2.6}$$

To improve background suppression, the ℓ_1-norm penalty weights were scaled from $r\lambda_1$ in background regions to λ_1 in vessels. To minimize vessel loss, the TV penalty weights were scaled from λ_2 in background regions to λ_2/r in vessels. The value of r was selected to maximize image contrast without introducing significant image distortions.

2.2.4.4 Phantom and in vivo reconstructions

For each dataset, separate Fourier (ZF), conventional CS and targeted CS (TCS) reconstructions were computed using parameters listed in Table 2.1. For ZF, data were compensated for k-space sampling density and inverse Fourier transformed. For CS, an identical $\lambda_2 = \lambda_{2o}$ was prescribed but several different λ_1 values were used. First conservative CS was performed using $\lambda_1 = \lambda_{1o}$ (CS_{low}). Second heavier penalization was performed using $\lambda_1 = 10\lambda_{1o}$ (CS_{high}). For phantom datasets, a separate CS was calculated with an even larger $\lambda_1 = \lambda_{1o,cont}$ (CS_{cont}), where λ_{cont} was selected to attain identical blood/background contrast to TCS. Because CS_{cont} caused severe image artifacts, it was omitted in subsequent analyses.

TCS was performed using $\lambda_{1,2} = \lambda_{1o,2o}$ and $r \in [1\ 20]$. For comparison, four other spatially-adaptive CS methods were employed with the same parameters. First an intensity-weighted reconstruction was performed using weight maps derived from the intensity of ZF (CS_{int}). ZF reconstructions were normalized to a maximum amplitude of unity and then inverted to calculate $W(i,j)$ similar to TCS. Second, iteratively-reweighted CS (CS_{IR}) was performed [61]. Weight maps for CS_{IR} were updated at each iteration based on the reconstruction at the previous iteration. Unlike TCS or CS_{int}, CS_{IR} maps did not reflect the region of signal support but rather the intensity of reconstructed images [61]. Finally, two separate variants of the TCS method were implemented to assess the relative importance of using spatially-adaptive weights on TV versus ℓ_1 penalties. The first variant TCS_{nTV} employed a spatially-weighted ℓ_1 and a fixed TV penalty, whereas the second variant $\mathrm{TCS}_{n\ell_1}$ employed a spatially-weighted TV and a fixed ℓ_1 penalty.

2.2.5 Simulations

To evaluate TCS independently from segmentation, we created two numerical phantoms that contained vessels immersed in a block of muscle tissue (Fig. 3.3a,c).

Both tissues were modeled with circular cross-sections. The first phantom contained 25 vessels of diameters ranging from 0.33 mm (1 pixel) to 2 mm (6 pixels). The vessels were arranged on a 5×5 rectilinear grid within a muscle block of diameter 100 mm (300 pixels). The second phantom contained 13 vessels of diameters between 1.25 to 3.75 mm, arranged randomly within the muscle block. Blood and muscle signals were simulated with the following parameters: $\alpha = 60^o$, $\mathrm{TR}_{l,s}$ = 3.45/1.15 ms, TE = 1.725 ms, $\mathrm{T}_1/\mathrm{T}_2$ = 1200/200 ms for blood [62] and 870/50 ms for muscle [5]. The phantom images were sampled with a 384×384 grid over a 128×128-mm^2 field-of-view. Circular cross-sections were created with a Fermi window using 1 pixel transition width. Finally, white Gaussian noise was added to yield a blood SNR of 20.

To examine penalty parameters used in TCS, we undersampled images of the first phantom with acceleration factors R = 1, 2, 4, 6 and 8. For each R, $\lambda_{1,2}$ values were ranged between 0 to 2 times the $\lambda_{1o,2o}$ values listed in Table 2.1. Meanwhile, the ratio (r) was varied in the range [1 20]. Larger TCS penalty weights yield improved background suppression (i.e., blood/muscle contrast), but cause distorted reconstructions of background signals. To assess reconstruction quality, a performance metric was calculated as the proportion of relative contrast difference to relative distortion level. Contrast improvement for each vessel was taken as:

$$\%\ \text{difference} = \frac{Cont_{TCS} - Cont_{ZF}}{\frac{1}{2}(Cont_{TCS} + Cont_{ZF})} \times 100 \tag{2.7}$$

Distortion level was taken as the normalized dispersion index of background tissue,

$$\Delta D = \frac{DI_{TCS}}{DI_{ZF}} \tag{2.8}$$

where $DI = \sigma^2/\mu$, and μ, σ denote the mean and standard deviation of the muscle signal, respectively.

TCS performance was assessed as a function of r (Fig. 3.3b), when $\lambda_{1,2} = \lambda_{1o,2o}$. Performance increases rapidly as r is initially raised above 1, and it saturates for relatively large r. Note that higher r enhances blood/background contrast at the expense of increased image distortions. Thus, for all R, $r = 10$ was selected that maintains more than 80% of the optimal performance. We then inspected

the performance for $r = 10$, $\lambda_1 = n\lambda_{1o}$ and $\lambda_2 = n\lambda_{2o}$ with n varying in the range [0 2]. Near optimal performance is attained for $\lambda_{1,2} = \lambda_{1o,2o}$. Independent optimizations of penalty weights indicate that $\lambda_{1,2} = \lambda_{1o,2o}$ and $r = 10$ yield close to optimal performance for $\mathrm{CS}_{int,IR}$ as well. Therefore, they were prescribed for all reconstructions hereafter. To examine the effects of vessel size, TCS was calculated for 20 independent instances of additive noise. As expected, smaller vessels -more susceptible to signal loss– exhibit greater contrast improvement with TCS.

Next, we assessed the benefits of TCS on the second phantom closely mimicking vessel sizes in the extremities [63]. Blood/muscle contrast and spatial resolution were compared across CS and TCS (Fig. 3.3c). Spatial resolution was taken as the FWHM sizes of individual blood vessels normalized by the prescribed sizes in the numerical phantom. Statistical differences were assessed with Wilcoxon signed-rank tests.

To investigate robustness against segmentation errors, separate TCS reconstructions were performed by simulating losses in segmented vessel maps (Fig. 3.3d). The ideal vessel masks were eroded to yield a volumetric loss varying between 0-30% of the total vessel volume. The erosion process used a random voxel selection that maintained spatial contiguity for each vessel. TCS was calculated for 20 distinct instances of vessel erosion and additive noise. Blood/muscle contrast and normalized vessel sizes were measured for each vessel individually and then averaged across 13 vessels.

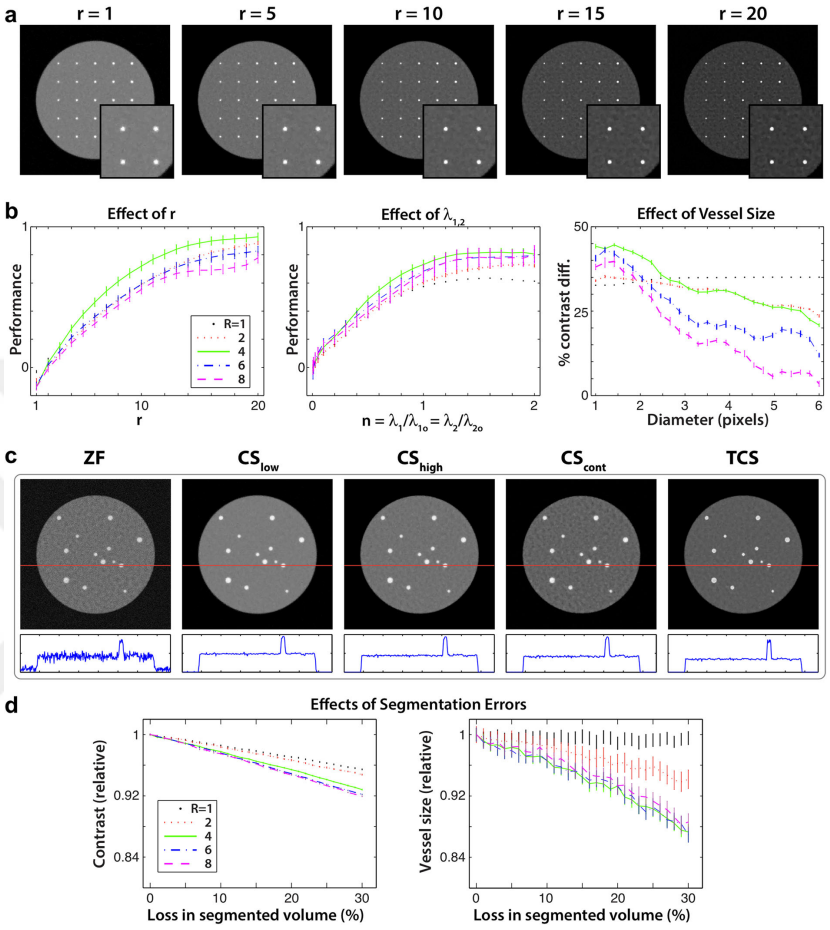

Figure 2.4: **(a)** A phantom with 25 blood vessels of sizes 0.33 to 2 mm enclosed by muscle. Targeted CS (TCS) reconstructions were calculated using $r \in [1\ 20]$, $\lambda_{1,2} = \lambda_{1o,2o}$, and R = 1-8. Results are shown for R = 4, with magnified lower-right portions of images. Higher r enhance blood/muscle contrast, but image distortions become prominent for $r \geq 15$. **(b)** TCS performance was taken as the ratio of contrast improvement to dispersion level (mean±sem across vessels). For all R, $r = 10$ and $\lambda_{1,2} = \lambda_{1o,2o}$ yield close to optimal reconstruction performance (left and middle panels). TCS using $\lambda_{1,2} = \lambda_{1o,2o}$ and $r = 10$ was repeated for 20 random instances additive noise. Contrast improvement is plotted for each vessel diameter (right panel; mean±sem across 20 images). The improvement is greater for smaller vessels. **(c)** A separate phantom with 13 blood vessels of sizes 1.25 to 3.75 mm. Fourier reconstructions (ZF), conventional CS, and TCS were calculated for R = 4. The panel below each image shows a sample line profile (across the red line). TCS improves blood/muscle contrast without significant image distortions. **(d)** TCS reconstructions were obtained while losses in segmented vessel maps were simulated by random erosions of the ideal map. Contrast and vessel sizes were measured relative to a TCS reconstruction based on the ideal map (mean±sem across 20 instances of erosion).

2.2.6 Experiments

To demonstrate TCS, we first acquired in vivo hand and lower-leg angiograms on a 1.5 T GE Signa EX scanner with CV/i gradients (maximum strength of 40 mT/m and slew rate of 150 T/m/s). High-resolution hand angiograms were collected in a healthy subject (male, age 27) using an 8-channel receive-only knee array, and with the following parameters: $0.5\times0.5\times0.5$-mm^3 spatial resolution, $320\times240\times120$ encoding matrix, $\alpha = 60^o$, $\mathrm{TR}_{l,s} = 3.6/1.2$ ms, TE = 1.8 ms, 125-kHz readout bandwidth, 80-ms T_2-preparation, 10-tip linear ramp catalyzation, 10 k-space segments, 4-s intersegment recovery time, and a total scan time of 3 min 40 s. Hand angiograms were retrospectively undersampled by acceleration factors of R = 1 (fully-sampled), 2, 4, 6 and 8. Data from each coil were reconstructed individually and sum-of-squares combined [64]. Meanwhile, prospectively undersampled lower-leg angiograms were collected in a healthy subject (female, age 28) using a transmit-receive quadrature extremity coil, and with identical parameters to the hand protocol except for: $1\times1\times1$-mm^3 spatial resolution, $192\times128\times128$ encoding matrix, $\mathrm{TR}_{l,s} = 3.45/1.15$ ms, TE = 1.725 ms. Separate acquisitions were performed at R = (1,2,4,6,8) with number of magnetization preparations N = (4,16,22,24,26) respectively, and scan time for each acquisition was 1 min 30 sec.

To validate TCS results in a broader population, we next collected lower-leg angiograms from 4 healthy subjects (1 female, 3 males; ages 27-32) and foot angiograms from 4 healthy subjects (2 females, 2 males; ages 27-30). Data were acquired on a 1.5 T GE Signa EX scanner using a quadrature extremity coil, with identical parameters to the lower-leg protocol listed above. The only exception was a fixed number of magnetization preparations N = 4 for all accelerations.

Vasculature maps were extracted from ZF reconstructions of undersampled data. CS and TCS reconstructions were then calculated on 2D cross sections. Reconstruction parameters were selected by examining TCS performance as a function of r and $\lambda_{1,2}$. It was observed that near-optimal performance is obtained

for $r = 10$ and $\lambda_{1,2} = \lambda_{1o,2o}$. To minimize partial volume effects in maximum-intensity projection (MIP) views, all reconstructed datasets were upsampled by a factor of two in all dimensions by zero-padding in k-space.

To assess image contrast, average blood and muscle signals were measured in 13 coronal cross-sections spanning across the entire volume. Within a single section, two separate regions-of-interest (ROIs) with homogeneous blood and muscle signal were selected. Signals were averaged within these ROIs, and ratio of blood to muscle signal was taken as the contrast for each cross-section. ROIs were identical across reconstructions of the same anatomy. In hand angiograms, blood signal was measured on superficial to deep segments of digital radial and ulnar arteries (569±142 voxels, mean±s.d. across 13 cross sections), muscle signal was measured in the palmar region (473±68 voxels). In lower-leg angiograms, blood signal was measured on proximal to distal segments of the tibial and peroneal arteries (73±20 voxels), muscle signal was measured across neighboring tissue (101±20). In foot angiograms, blood signal was measured on dorsal metatarsal and plantar arteries (52±34 voxels), and muscle signal was measured across neighboring tissue (80±29).

To examine potential blurring artifacts, vessel thickness measurements were performed in hand and lower leg datasets. For this analysis, vessels of various sizes were selected across 10 different axial cross-sections. The thickness of each vessel was taken as the diameter of the FWHM region, which ranged from 1 to 4 mm. The level of blurring in each reconstruction method was calculated as the relative vessel diameter compared to a ZF reconstruction of fully-sampled data (R = 1).

Two expert radiologists evaluated the diagnostic quality of reconstructed images by consensus. At each R, MIP views were used to compare images from different reconstruction methods (without method identifiers). Image contrast, vessel demarcation and distal-branch visualization in each image were separately rated using a five point scale (5 excellent, 4 good, 3 moderate, 2 limited, 1 poor). Statistical differences in quantitative measurements and rating scores were assessed with Wilcoxon signed-rank tests.

2.3 Results

Blood/muscle contrast and resolution on simulated phantom images are listed in Table 2.2. At each R, TCS significantly improves contrast compared to all other methods including TCS_{nTV} and $\text{TCS}_{n\ell_1}$ ($P < 0.05$). We find an improvement of 21.5±8.7% over CS_{low} (mean±s.d. across R) and 11.3±2.8% over CS_{IR}, the closest CS competitor to TCS. The contrast improvement is greater for lower R values, where heavier sparsity penalties can be enforced due to increased acquisition SNR. Furthermore, TCS maintains improved spatial resolution compared to other CS methods and $\text{TCS}_{n\ell_1}$ at each R ($P < 0.05$). This improvement in resolution is more prominent in higher R datasets that are more susceptible to resolution loss.

To assess the reliability of TCS against segmentation errors, phantom images were reconstructed for varying volumetric losses in vessel maps. TCS using randomly eroded versions of the ideal vessel map was compared to TCS using the ideal map (Fig. 3.3d). At all R values, contrast remains within 8% and vessel size remains within 12% of their ideal values for up to 30% segmentation loss. These results indicate that TCS shows considerable performance in the presence of moderate segmentation errors.

Table 2.2: Contrast and Resolution: Simulated data

Contrast

		R = 1	**R = 2**	**R = 4**	**R = 6**	**R = 8**
ZF	Cont.	1.89	1.88	1.86	1.87	1.87
	% diff.	-	-	-	-	-
CS$_{low}$	Cont.	1.91	1.89	1.88	1.88	1.88
	% diff.	0.9%	0.9%	1.1%	0.9%	0.5%
CS$_{high}$	Cont.	2.27	2.11	2.02	1.95	1.91
	% diff.	18.2%	11.6%	8.1%	4.3%	2.4%
CS$_{int}$	Cont.	2.18	2.04	2.00	1.94	1.90
	% diff.	14.2%	8.5%	6.9%	3.7%	1.9%
CS$_{IR}$	Cont.	2.36	2.25	2.06	1.94	1.90
	% diff.	22.3%	18.1%	9.9%	3.7%	1.7%
TCS$_{nTV}$	Cont.	2.67	2.40	2.30	2.18	2.08
	% diff.	34.2%	24.2%	21.2%	15.4%	10.9%
TCS$_{n\ell_1}$	Cont.	2.29	2.13	2.04	1.97	1.93
	% diff.	19.2%	12.4%	9.0%	5.3%	3.3%
TCS	Cont.	2.69	2.41	2.33	2.21	2.11
	% diff.	35.0%	25.0%	22.5%	16.7%	12.4%

Resolution

	R = 1	**R = 2**	**R = 4**	**R = 6**	**R = 8**
ZF	1.09±0.05	1.12±0.06	1.27±0.14	1.36±0.21	1.42±0.29
CS$_{low}$	1.05±0.04	1.08±0.05	1.09±0.06	1.08±0.06	1.17±0.09
CS$_{high}$	1.06±0.05	1.09±0.06	1.10±0.07	1.09±0.06	1.15±0.10
CS$_{int}$	1.07±0.04	1.11±0.06	1.17±0.09	1.16±0.08	1.18±0.12
CS$_{IR}$	1.07±0.04	1.06±0.05	1.16±0.08	1.18±0.08	1.20±0.12
TCS$_{nTV}$	1.00±0.01	1.01±0.02	1.00±0.01	0.99±0.01	0.99±0.02
TCS$_{n\ell_1}$	1.05±0.04	1.08±0.05	1.09±0.05	1.06±0.05	1.12±0.08
TCS	1.00±0.01	1.01±0.01	1.00±0.01	0.98±0.02	0.98±0.02

Contrast: Average blood/muscle contrast on phantom data at various R. Raw contrast values are listed together with the percentage difference in contrast between each method and ZF. *Resolution:* Relative radius of blood vessels in phantom images (mean±s.d. across 13 vessels) compared to the actual vessel sizes.

Representative reconstructions of in vivo hand and lower-leg angiograms are shown in Figs. 2.5-2.7. TCS visibly improves blood/background contrast and enhances vessel depiction via tailored penalty weights. Note that we find no significant differences in vessel thickness across reconstructions methods and across R ($P > 0.125$). Thus the prominent appearance of vessel trees in TCS reconstructions is due to improved angiographic contrast. While some small vessels are less effectively visualized at $R \geq 6$ due to reduction of segmented volumes (Fig. 2.3), TCS reliably depicts major vessels including the digital-radial/ulnar arteries in the hand, and popliteal/peroneal arteries in the lower leg. Blood/background contrast measurements in representative hand and lower-leg angiograms are listed in Table 2.3 and Table 2.4. At each R, TCS yields significantly higher contrast than all other methods including TCS_{nTV} and $\text{TCS}_{n\ell_1}$ ($P < 0.05$). In the hand, the improvement is 71.3±28.9% over CS_{low} and 33.0±6.6% over CS_{IR}. In the lower leg, the improvement is 38.5±8.5% over CS_{low} and 22.1±6.6% over CS_{IR}.

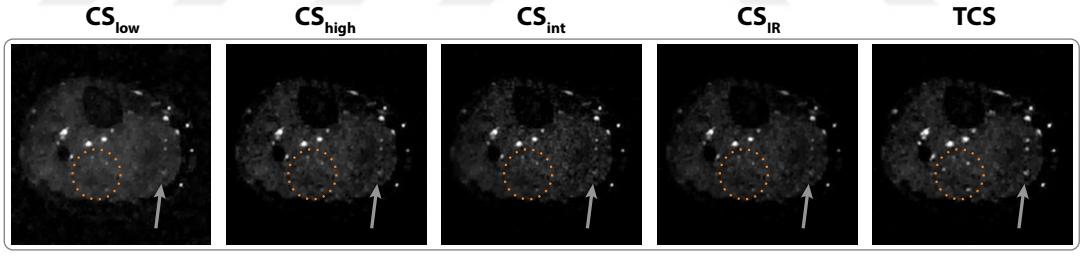

Figure 2.5: Lower-leg angiograms reconstructed using conventional CS with uniformly-weighted penalty terms (CS_{low}, CS_{high}), CS with spatially-weighted penalty terms based on intensity of ZF reconstructions (CS_{int}), iteratively-reweighted CS (CS_{IR}), and TCS. Representative axial sections are shown for $R = 4$. CS_{high}, CS_{int} and CS_{IR} suffer from signal losses, particularly in relatively small or low intensity vessels. In contrast, TCS improved background suppression while preserving detailed depiction of vasculature (marked with ellipses and arrows).

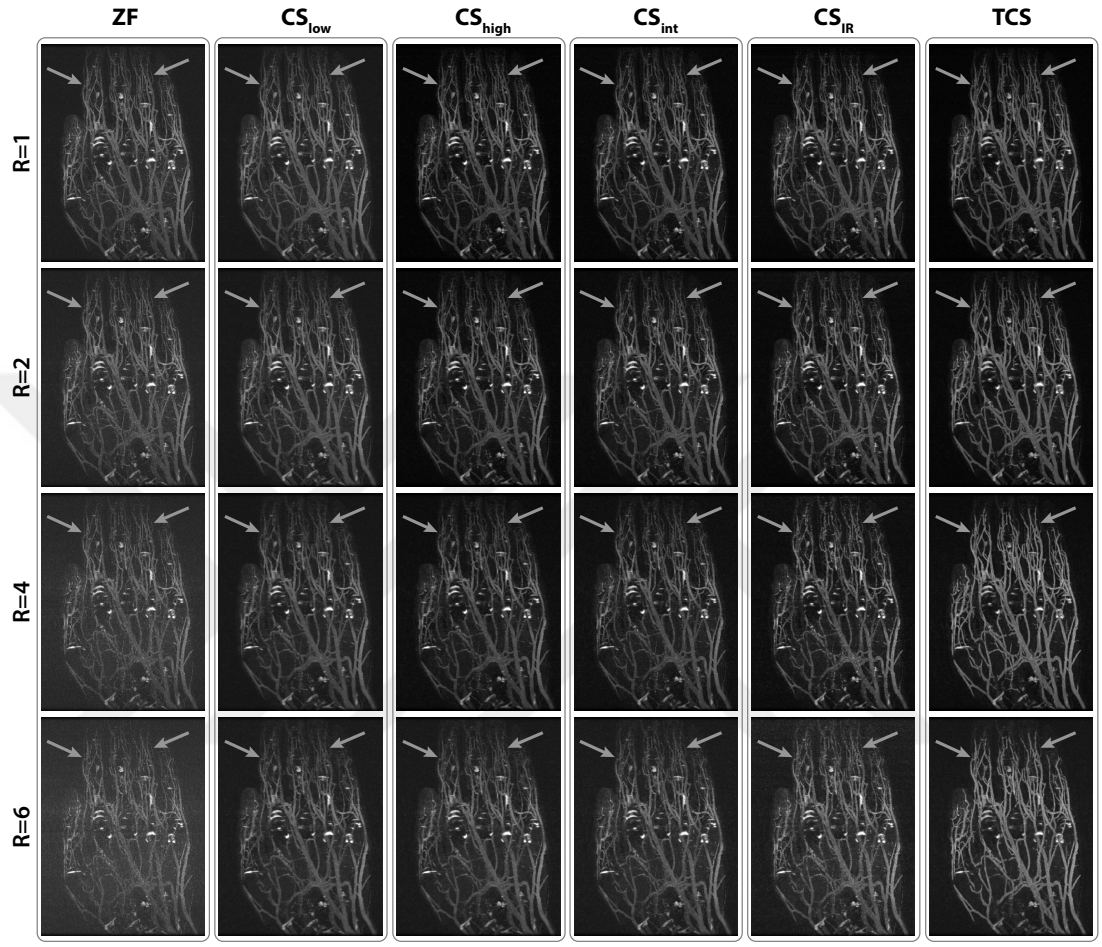

Figure 2.6: MIPs of hand angiograms reconstructed with ZF, CS_{IR} and TCS, for R = 1-6. CS_{IR} suffers increasingly from loss of small vessels for higher R. Furthermore, bright synovial fluid causes suboptimal vessel contrast in ZF and CS_{IR}. In contrast, TCS alleviates vessel loss while improving suppression of background signals (marked with arrows).

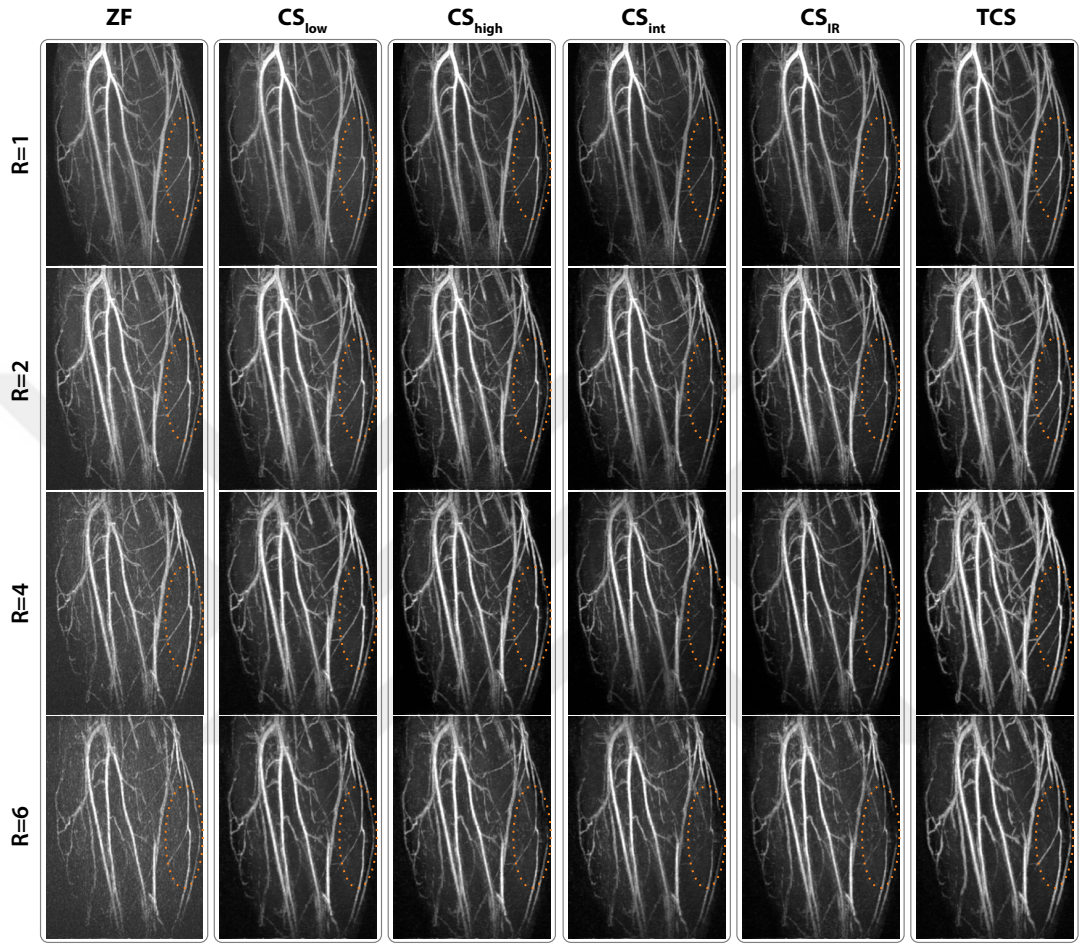

Figure 2.7: MIPs of lower leg angiograms reconstructed with ZF, CS_{IR} and TCS, for R = 1-6. There is visible loss of low-intensity and small vessels in CS_{IR}. TCS achieves improved blood/muscle contrast with no visible vessel loss up to R = 4 (marked with ellipses). Due to reduction of segmented volumes for R = 6 (Fig. 2.3), some small vessels are depicted suboptimally.

The contrast measurements in lower-leg and foot angiograms collected in a population of 8 subjects are listed in Table 2.5 and Table 2.6. Across subjects, TCS achieves higher contrast than all other reconstructions at each R ($P < 0.05$). In the lower leg, the improvement is 30.6±11.3% over CS_{low}, 13.8±2.7% over CS_{IR}, 3.0±1.4% over TCS_{nTV} and 13.8±2.7% over $TCS_{n\ell_1}$. In the foot, the improvement is 28.1±7.0% over CS_{low}, 14.9±1.8% over CS_{IR}, 3.0±1.5% over

TCS_{nTV} and 11.4±2.6% over $\text{TCS}_{n\ell_1}$. Consistent with simulation results, contrast improvement for in vivo data is greater for lower R.

Radiological assessments of image contrast, vessel demarcation, and distal-branch visualization concur that the proposed method enhances image quality (see Table 2.7). Across all subjects, TCS achieves higher image contrast and vessel demarcation scores than all other CS reconstructions at each R ($P < 0.05$), except for R = 1 where we find no significant difference. While comparisons are less uniform for distal-branch visualization, the average visualization score across R is higher for TCS compared to all other reconstructions ($P < 0.05$).

Table 2.3: Contrast: Representative Single-Subject Hand Data

		R = 1	**R = 2**	**R = 4**	**R = 6**	**R = 8**
ZF	Cont.	2.32±0.10	2.25±0.10	2.06±0.12	2.02±0.13	2.01±0.12
	% diff.	-	-	-	-	-
CS_{low}	Cont.	2.35±0.11	2.23±0.11	2.04±0.09	1.97±0.10	2.00±0.08
	% diff.	1.35%	-1.14%	-0.82%	-2.86%	-0.11%
CS_{high}	Cont.	6.92±0.87	3.55±0.29	2.62±0.14	2.08±0.12	2.11±0.09
	% diff.	99.63%	44.83%	23.79%	2.96%	5.06%
CS_{int}	Cont.	5.50±0.55	3.45±0.27	2.70±0.14	2.17±0.12	2.18±0.09
	% diff.	81.51%	42.12%	26.97%	6.83%	8.58%
CS_{IR}	Cont.	5.63±0.65	3.71±0.31	3.03±0.16	2.38±0.15	2.41±0.11
	% diff.	83.38%	49.08%	38.00%	16.12%	18.28%
TCS_{nTV}	Cont.	8.56±1.03	4.80±0.37	4.03±0.21	2.86±0.18	2.91±0.13
	% diff.	114.79%	72.30%	64.72%	34.34%	36.69%
$\text{TCS}_{n\ell_1}$	Cont.	7.19±0.87	3.73±0.31	2.87±0.15	2.36±0.13	2.40±0.10
	% diff.	102.56%	49.55%	32.73%	15.22%	17.92%
TCS	Cont.	8.70±1.04	4.99±0.38	4.30±0.22	3.16±0.21	3.22±0.15
	% diff.	115.89%	75.64%	70.51%	44.05%	46.50%

Blood/muscle contrast (mean±s.d. across 13 sections) in hand angiograms at various R. Raw contrast values are listed together with the percentage difference in contrast between each method and ZF.

Table 2.4: Contrast: Representative Single-Subject Lower Leg Data

		R = 1	**R = 2**	**R = 4**	**R = 6**	**R = 8**
ZF	Cont.	1.82±0.24	2.11±0.27	2.24±0.14	2.61±0.18	2.74±0.20
	% diff.	-	-	-	-	-
CS$_{low}$	Cont.	1.84±0.27	2.13±0.32	2.31±0.20	2.66±0.20	2.72±0.32
	% diff.	1.06%	1.08%	2.95%	2.06%	-0.49%
CS$_{high}$	Cont.	2.52±0.59	2.68±0.57	2.71±0.31	2.79±0.24	2.81±0.41
	% diff.	31.90%	23.83%	19.18%	6.67%	2.79%
CS$_{int}$	Cont.	2.46±0.48	2.69±0.55	2.79±0.30	2.85±0.20	2.85±0.28
	% diff.	29.66%	24.36%	22.05%	8.91%	4.19%
CS$_{IR}$	Cont.	2.50±0.58	2.74±0.59	2.77±0.36	2.87±0.28	2.79±0.45
	% diff.	31.24%	26.22%	21.29%	9.47%	1.80%
TCS$_{nTV}$	Cont.	3.04±0.69	3.11±0.65	3.28±0.39	3.30±0.31	3.57±0.50
	% diff.	50.03%	38.46%	37.84%	23.37%	26.51%
TCS$_{n\ell_1}$	Cont.	2.57±0.60	2.76±0.58	2.84±0.32	2.99±0.27	3.10±0.45
	% diff.	34.11%	26.72%	23.70%	13.65%	12.58%
TCS	Cont.	3.11±0.70	3.17±0.65	3.42±0.40	3.52±0.34	3.88±0.54
	% diff.	52.08%	40.28%	41.62%	29.76%	34.63%

Blood/muscle contrast (mean±s.d. across 13 sections) in lower leg angiograms at various R. Raw contrast values are listed together with the percentage difference in contrast between each method and ZF.

Table 2.5: Contrast: Population Lower Leg Data

		R = 1	**R = 2**	**R = 4**	**R = 6**	**R = 8**
ZF	Cont.	2.19±0.28	2.17±0.28	2.12±0.27	2.08±0.25	2.04±0.25
	% diff.	-	-	-	-	-
CS$_{low}$	Cont.	2.21±0.29	2.17±0.30	2.10±0.30	2.05±0.29	2.02±0.31
	% diff.	1.2±0.8%	-0.1±1.3%	-1.1±2.0%	-1.9±2.9%	-1.4±4.1%
CS$_{high}$	Cont.	2.99±0.43	2.68±0.38	2.39±0.37	2.12±0.31	2.07±0.31
	% diff.	30.8±6.2%	20.7±3.5%	11.6±3.2%	1.7±3.4%	1.3±3.9%
CS$_{int}$	Cont.	3.00±0.58	2.71±0.44	2.41±0.41	2.13±0.32	2.08±0.32
	% diff.	30.6±8.7%	21.5±4.5%	12.4±4.5%	2.0±3.6%	1.5±4.0%
CS$_{IR}$	Cont.	3.02±0.48	2.76±0.42	2.50±0.43	2.14±0.32	2.08±0.32
	% diff.	31.7±7.3%	23.6±5.3%	15.8±4.7%	2.7±3.9%	1.9±4.1%
TCS$_{nTV}$	Cont.	3.41±0.45	3.10±0.38	2.87±0.36	2.37±0.30	2.34±0.29
	% diff.	43.6±8.8%	35.2±5.9%	30.0±3.8%	12.9±3.4%	13.8±3.7%
TCS$_{n\ell_1}$	Cont.	3.03±0.44	2.73±0.37	2.48±0.37	2.21±0.30	2.17±0.30
	% diff.	32.4±6.6%	22.8±4.3%	15.2±2.9%	6.0±3.0%	6.1±3.3%
TCS	Cont.	3.46±0.45	3.15±0.36	2.97±0.35	2.47±0.29	2.45±0.28
	% diff.	45.0±8.1%	36.9±6.6%	33.4±4.6%	17.0±3.9%	18.5±4.2%

Blood/muscle contrast (mean±s.d. across 4 subjects) in lower-leg angiograms at various R. Raw contrast values are listed together with the percentage difference in contrast between each method and ZF.

Table 2.6: Contrast: Population Foot Data

		$\mathbf{R = 1}$	$\mathbf{R = 2}$	$\mathbf{R = 4}$	$\mathbf{R = 6}$	$\mathbf{R = 8}$
ZF	Cont.	2.45±0.23	2.41±0.20	2.31±0.19	2.21±0.16	2.08±0.15
	% diff.	-	-	-	-	-
$\mathbf{CS}_{low}$	Cont.	2.49±0.23	2.44±0.24	2.35±0.26	2.27±0.26	2.18±0.27
	% diff.	1.7±0.2%	1.1±1.5%	1.6±4.3%	2.2±5.1%	4.7±6.8%
$\mathbf{CS}_{high}$	Cont.	3.21±0.28	2.98±0.21	2.71±0.27	2.39±0.27	2.29±0.29
	% diff.	27.2±3.3%	21.0±3.7%	15.9±5.4%	7.2±5.6%	9.3±7.2%
$\mathbf{CS}_{int}$	Cont.	3.25±0.22	3.06±0.17	2.79±0.17	2.44±0.21	2.34±0.22
	% diff.	28.4±4.6%	23.8±5.2%	19.1±5.1%	9.7±4.8%	12.0±5.2%
$\mathbf{CS}_{IR}$	Cont.	3.41±0.19	3.14±0.17	2.83±0.18	2.45±0.21	2.34±0.25
	% diff.	33.1±5.0%	26.3±6.7%	20.6±5.8%	10.1±5.0%	11.6±6.3%
$\mathbf{TCS}_{nTV}$	Cont.	3.49±0.29	3.30±0.18	3.18±0.17	2.65±0.23	2.58±0.27
	% diff.	35.2±4.6%	31.1±6.7%	31.9±6.5%	17.9±6.4%	21.3±7.3%
$\mathbf{TCS}_{n\ell_1}$	Cont.	3.25±0.28	3.03±0.20	2.79±0.25	2.49±0.25	2.40±0.27
	% diff.	28.1±3.9%	22.8±4.2%	18.9±5.5%	11.6±5.7%	14.4±6.8%
TCS	Cont.	3.54±0.30	3.37±0.17	3.26±0.16	2.76±0.23	2.71±0.26
	% diff.	36.6±5.1%	33.1±6.6%	34.4±7.4%	22.0±7.4%	26.3±8.0%

Blood/muscle contrast (mean±s.d. across 4 subjects) in foot angiograms at various R. Raw contrast values are listed together with the percentage difference in contrast between each method and ZF.

Table 2.7: Radiological Assessment of Image Quality

Image Contrast

	R = 1	**R = 2**	**R = 4**	**R = 6**	**R = 8**
ZF	4.1±0.1	4.1±0.1	3.5±0.2	2.7±0.2	2.1±0.2
CS$_{low}$	4.1±0.1	4.1±0.1	3.9±0.1	3.4±0.2	3.1±0.2
CS$_{high}$	4.5±0.2	4.1±0.2	3.6±0.2	3.4±0.2	3.1±0.2
CS$_{int}$	4.4±0.2	3.9±0.2	3.2±0.3	3.0±0.3	2.8±0.3
CS$_{IR}$	4.4±0.2	3.9±0.2	3.4±0.3	3.3±0.2	3.1±0.2
TCS	4.8±0.1	4.8±0.2	4.7±0.2	4.2±0.2	4.1±0.2

Vessel Demarcation

	R = 1	**R = 2**	**R = 4**	**R = 6**	**R = 8**
ZF	4.6±0.2	4.3±0.3	3.5±0.3	3.2±0.3	2.5±0.4
CS$_{low}$	4.6±0.2	4.4±0.2	3.7±0.2	3.3±0.3	2.5±0.2
CS$_{high}$	4.7±0.2	4.5±0.2	3.8±0.2	3.3±0.3	2.6±0.2
CS$_{int}$	4.6±0.2	4.4±0.2	3.7±0.2	3.2±0.3	2.4±0.3
CS$_{IR}$	4.6±0.2	4.5±0.2	3.8±0.2	3.2±0.3	2.5±0.2
TCS	5.0±0.0	5.0±0.0	4.9±0.1	4.4±0.2	3.9±0.2

Distal-Branch Visualization

	R = 1	**R = 2**	**R = 4**	**R = 6**	**R = 8**
ZF	4.6±0.2	4.5±0.2	3.7±0.2	2.9±0.3	2.2±0.3
CS$_{low}$	4.6±0.2	4.6±0.2	3.9±0.2	3.6±0.3	3.0±0.2
CS$_{high}$	4.3±0.2	4.4±0.2	3.5±0.2	3.6±0.3	3.0±0.2
CS$_{int}$	4.3±0.2	4.3±0.2	3.3±0.2	3.4±0.3	2.9±0.2
CS$_{IR}$	3.9±0.3	3.8±0.2	3.2±0.2	3.6±0.3	3.1±0.2
TCS	4.5±0.2	4.6±0.2	4.3±0.2	4.0±0.2	3.9±0.2

Rating scores for image contrast, vessel demarcation, and distal-branch visualization (mean±s.e.m. across 10 subjects).

2.4 Discussion

Here we propose a reconstruction strategy (TCS) for NCE angiograms that leverages vasculature maps extracted from undersampled data, without relying on prior information. The morphological information in these maps is used to apply order-of-magnitude heavier sparsity and TV penalties across background tissues compared to vessels. As such, TCS enhances blood/background contrast compared to conventional CS without degrading vessel depiction.

A recent study has used 2D segmentations to apply a spatially-varying ℓ_1-penalty [49]. While this previous approach has similar motivations to TCS, our study differs in several important aspects. First, we use a tractographic segmentation to exploit 3D structure and leverage vessel contiguity in the superior-inferior direction. Second, we utilize concurrent spatial-weighting on both ℓ_1-norm and TV penalties to minimize vessel signal loss. Our results show that concurrent weighting in TCS enhances image quality over weighting either term alone. Lastly apart from noise/aliasing reduction aimed previously, here we demonstrate contrast enhancement that significantly improves vessel depiction in contrast-limited NCE MRA.

Practical benefits of TCS depend on the coverage of the segmented vasculature maps. Our simulations suggest that TCS maintains considerable performance with up to 30% volume loss in segmented maps. However with increased aliasing at high R, small vessels with low contrast may be missed and thereby incur heavy penalties during TCS. Here some small, low-contrast branches were not segmented at R = 6 and 8; and loss of high-spatial-frequency information in TCS became prominent at R = 8 (not shown). Such losses may mimic stenoses in minor vessel branches. To minimize misassessment, segmented maps can be more broadly dilated and reconstruction penalties may be limited at higher R. Alternatively, segmentation and reconstruction stages can be cast as a joint optimization problem [65], with iterative refinement across both stages. These demanding optimizations can be completed in practical run times using graphical processing units [66, 67].

With heavier undersampling, it will become challenging to distinguish vessel signals from aliasing/noise interference. Higher R can be attained for TCS by improving SNR, blood/background contrast and spatial resolution of angiographic acquisitions. These improvements will boost both segmentation and reconstruction performances. Furthermore, increased spatial resolution can also enhance the delineation of vessel boundaries during segmentation. Here we prescribed relatively high spatial resolution (e.g. 0.5 mm for hand), and used a segmentation that can detect a minimum lumen size equal to this resolution. However, delineation of small, distal vessels might be impaired at more limited spatial resolutions. In such cases, parallel imaging and CS techniques can be combined to alleviate resolution limitations [9, 68].

TCS applies first-order finite difference operators to incur a TV penalty. Penalty weights were kept low here to minimize block artifacts, and no significant distortions were observed around vessels. However, higher-order TV terms may enable better denoising in piece-wise smooth regions while preserving edge information near vessel boundaries [69]. Another improvement for TCS concerns the sparsity penalties applied in the image domain. While angiographic images are natively sparse, spatially-weighted penalties in relevant sparsifying transform domains (e.g. wavelet domain) might be needed for other applications. Adaptive wavelet-domain penalties have been previously designed based on manual ROI specifications [46] or dependencies between wavelet coefficients [70]. Similarly, TCS with spatially-weighted wavelet penalties may be useful in applications such as coronary imaging.

Residual signals from several background tissues are evident in FIA datasets. First, synovial fluid in the joints with relatively high T_2/T_1 ratio yields comparable bSSFP signal to vessels. While our segmentations correctly classify synovial fluid as background, excessive reconstruction penalties are required to fully dampen these bright signals. If further suppression is desired, synovial fluid maps can be manually segmented to apply higher penalty weights compared to other background tissues. Second, the vessel maps presented here contain both arterial and venous streams in the peripheral extremities. Because the two streams may be located closely, segmentation algorithms can assign venous voxels onto

arterial vessels [71]. For improved separation, segmentation maps can be manually corrected to exclude residual venous tissue. Alternatively, the segmentation method can be modified to leverage smoothness of surface curvature and fuzzy connectedness to delineate arterial and venous trees [72, 71, 54].

In conclusion, the two-step TCS method outperforms regular CS methods in angiographic reconstructions consistently across subjects. While the proposed method was successfully demonstrated for peripheral FIA, it can easily be extended to other angiographic acquisitions. These promising results warrant future studies on a clinical population that examine pathological cases including abrupt occlusions and small stenotic vessels.

Chapter 3

Profile encoding reconstruction for multiple-acquisition balanced steady-state free precession imaging

This chapter is based on publication 'Profile-encoding reconstruction for multiple-acquisition balanced steady-state free precession imaging.', Ilicak, E., Senel, L. K., Biyik, E. and and Çukur, T., Magn. Reson. Med., 2016.

List of Abbreviations

C_n	bSSFP profile
S_n	Phase-cycled image
S_o	Artifact-free image
y_{calib}	Calibration data (fully-sampled part of central k-space)
y_n	Phase-cycled data for nth acquisition
bSSFP	Balanced steady-state free precession
CS	Compressed sensing
ESPIRiT	Eigenvalue Approach to Autocalibrating Parallel MRI
FOV	Field-of-view
iCS	Individual-CS reconstruction
N	Number of phase-cycles
PE-SSFP	Profile-Encoding SSFP reconstruction
PE$_{calib}$	PE reconstruction with calibration and data-consistency projections
PE$_{huber}$	PE reconstruction with Huber thresholding in addition to PE$_{calib}$
PE$_{soft-TV}$	PE reconstruction with soft thresholding in addition to PE$_{calib}$
PSNR	Peak SNR
R	Acceleration factor
SNR	Signal-to-noise ratio
SPIRiT	Iterative self-consistent parallel imaging
SSIM	Structural similarity index
TE	Echo time
TR	Repetition time
TV	Total-variation
VD	Variable-density
ZF	Zero-filled Fourier

3.1 Introduction

Balanced steady-state free precession (bSSFP) sequences provide relatively high magnetization levels for repetition times (TR) on the order of several milliseconds [73]. As such, they have found use in rapid imaging involving both dynamic [74, 75, 76, 77, 78] and high-spatial-resolution static acquisitions [28, 30, 31, 79, 37]. One critical concern, however, is that the bSSFP magnetization profile yields increased sensitivity to magnetic field inhomogeneities and signal voids at particular off-resonance frequencies [73]. In turn, this profile can lead to excessive banding artifacts at high field strengths, with long TRs, and in complex tissue geometries.

Several innovative methods were previously proposed to alleviate bSSFP banding artifacts. These methods include modified pulse sequences that reshape magnetization profiles [80, 81, 82, 83], advanced shimming procedures that limit field inhomogeneity [84], physical signal models to remove frequency sensitivity [85, 86], and the commonly used multiple-acquisition methods that combine several phase-cycled images with nonoverlapping banding artifacts to improve signal homogeneity [87, 88, 89, 29, 90, 91]. These approaches typically compromise between artifact reduction and scan efficiency. For instance, residual banding artifacts in multiple-acquisition methods can be reduced by increasing the number of phase cycles (N). However, with higher N, the overall scan time is considerably prolonged.

To mitigate banding artifacts while maintaining scan efficiency, two recent studies proposed to accelerate phase-cycled bSSFP acquisitions [32, 92]. In the first study [32], we leveraged individual compressed-sensing (CS) reconstructions to recover nonacquired bSSFP data for each phase cycle separately [39, 4, 8]. In the second study [92], individual acquisitions were instead accelerated via simultaneous multi-slice imaging. While high image quality was demonstrated for low acceleration factors (around 2-4), data from separate phase-cycles were reconstructed independently in both studies. Because independent reconstructions

ignore structural information that is inherently correlated across multiple acquisitions [68, 9, 93], image quality can be degraded at high acceleration factors that are critically needed with increasing N.

Here, we propose an improved framework for accelerating phase-cycled bSSFP imaging that jointly reconstructs undersampled data across multiple acquisitions. Analogous to parallel imaging that takes each coil image as the product of the tissue image with a respective coil sensitivity [94], this framework models each phase-cycled bSSFP image as the product of the banding-artifact-free image with a respective bSSFP spatial profile [95, 96]. Thus, inspired by recent approaches for multi-coil imaging [93], the joint reconstruction is cast as a profile-encoding problem (PE-SSFP) where nonacquired k-space samples are linearly synthesized from acquired data. To further alleviate aliasing and noise interference, PE-SSFP leverages joint-sparsity and total-variation penalties. Comprehensive simulations are presented to demonstrate the reliability of PE-SSFP against variations in sequence and tissue parameters, noise, and field inhomogeneity. Phantom and in vivo results clearly indicate that the proposed framework yields improved image quality over conventional reconstructions.

3.2 Methods

The goal of the current study is to implement robust, artifact-free multiple-acquisition bSSFP imaging within a total scan time equivalent to a single acquisition. Starting with an overview of phase-cycled bSSFP imaging, the following sections discuss the sampling and reconstruction strategies proposed towards this goal.

Multiple-Acquisition Phase-Cycled bSSFP Imaging

In multiple-acquisition bSSFP, several images with different phase-cycling are acquired such that banding artifacts are spatially non-overlapping across acquisitions. Assuming TE=TR/2, the fully-sampled images at each phase cycle can be expressed as [97]:

$$S_n(r) = M(r)\frac{e^{i(\phi(r)+\Delta\phi_n)/2}\left(1 - A(r)e^{-i(\phi(r)+\Delta\phi_n)}\right)}{1 - B(r)\cos(\phi(r)+\Delta\phi_n)} \tag{3.1}$$

where r denotes spatial location, $\phi(r)$ is phase accrued in a single TR due to field inhomogeneity, and $\Delta\phi_n$ is the phase-cycling value used for the n^{th} acquisition where $n \in [1\ \mathrm{N}]$. The remaining terms M, A, B depend on sequence and tissue parameters. Tailored image combination techniques are then used to minimize the dependence of the bSSFP signal on $\phi(r)$ [88, 29]. An artifact-free image (S_o) could be obtained under the condition that $\phi(r) + \Delta\phi_n = \pi$, which in turn would yield:

$$S_o(r) = iM(r)\frac{1 + A(r)}{1 + B(r)} \tag{3.2}$$

Thus, each phase-cycled image S_n can be modeled as the multiplication of S_o with a respective bSSFP profile, C_n as illustrated in Fig. 3.1:

$$C_n(r) = \frac{S_n(r)}{S_o(r)} = \frac{e^{i(\phi+\Delta\phi_n-\pi)/2}\,(1+B)\left(1 - Ae^{-i(\phi+\Delta\phi_n)}\right)}{(1+A)(1 - B\cos(\phi+\Delta\phi_n))} \tag{3.3}$$

Combination techniques for multiple-acquisition bSSFP typically assume that data are either fully-sampled [88, 89, 29] or else adequately reconstructed [32]. Estimation of bSSFP profiles has therefore not been of particular interest, apart from cases where signal-to-noise ratio (SNR) optimization or fat-water separation is aimed [95, 90]. Nonetheless, the bSSFP profiles can be interpreted as a means to perform spatial encoding [96], similar to that implemented by the coil sensitivities in parallel imaging [94]. With this interpretation, we cast the joint reconstruction of undersampled phase-cycled acquisitions as a profile-encoding problem:

$$y_n(k) = \mathcal{F}_n\left\{C_n(r) \cdot S_o(r)\right\} \tag{3.4}$$

Here k indicates k-space location, y_n are the k-space data for the n^{th} acquisition, and $\mathcal{F}$ is a Fourier-transform operator. For simplicity, we did not consider the

effects of coil sensitivities on the joint reconstruction. Thus, assuming that bSSFP spatial profiles can be estimated based on fully-sampled central k-space data [98, 99], they can be used to solve an inverse problem that recovers the artifact-free bSSFP image $S_o(r)$ given a collection of phase-cycled data $y_n(k)$.

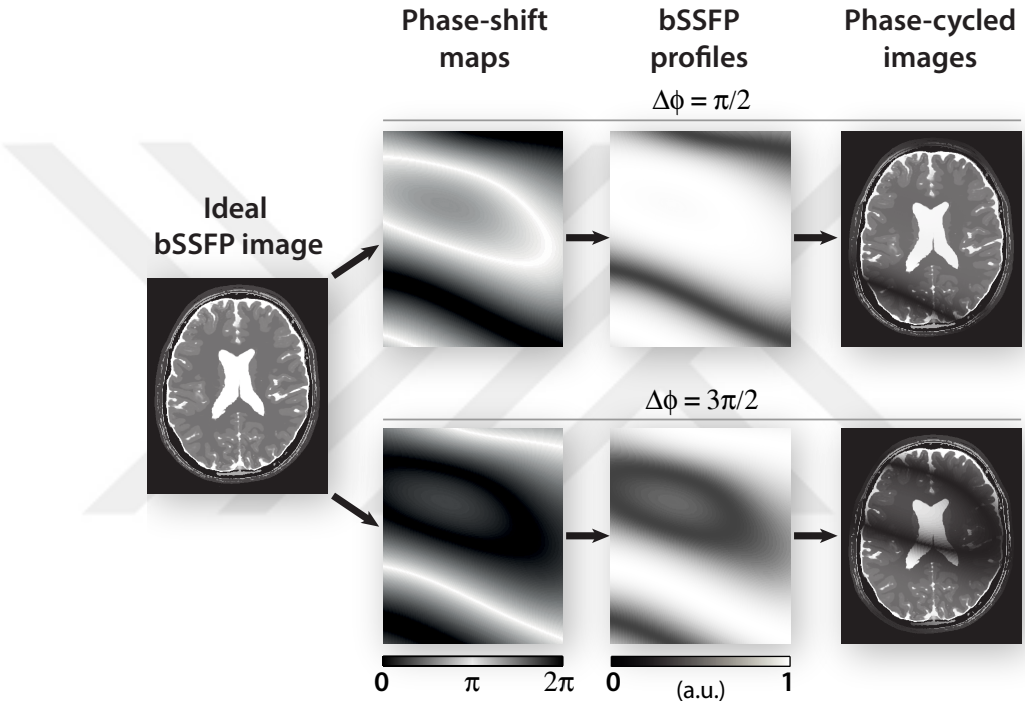

Figure 3.1: In the profile-encoding framework, each phase-cycled bSSFP image (S_n) is modeled as the multiplication of an ideal image free of banding artifacts (S_o) with a respective bSSFP sensitivity profile (C_n). The value of the bSSFP profile at each location is a function of total phase accrual over a single TR due to main field inhomogeneity and RF phase-cycling increment ($\Delta\phi$). Locations of near-zero phase shift (modulo 2π) lead to significantly diminished sensitivity and thereby banding artifacts in bSSFP images.

3.2.1 Undersampling Patterns for Multiple-Acquisition bSSFP Data

Each of N separate phase-cycled acquisitions were undersampled by a factor of R=N. Sampling patterns for phase-cycled acquisitions can be selected independently. A common pattern for all acquisitions can better enforce consistency in the sampling matrix across phase-cycles, and reduce interpolation errors. On the other hand, disjoint patterns across acquisitions can expand k-space coverage, and reduce aliasing artifacts [32]. To optimize sampling strategy, we compared reconstructions of data undersampled with common versus disjoint patterns. Patterns were generated using uniform-density deterministic [94, 96], variable-density random [4], and Poisson-disc sampling [93]. In all cases, isotropic acceleration was performed in two dimensions, and a central k-space region spanning up to 10% of the maximum spatial frequency in each axis was fully sampled. In uniform-density sampling, the full sampling matrix was linearly ordered and then undersampled by holding every N^{th} sample (e.g., 1, N+1,...). Disjoint patterns were generated by incrementing the starting index by 1 sample [96]. In variable-density sampling, random patterns were generated based on a polynomial probability density function (PDF), and sampling patterns were selected among 2000 candidate patterns to minimize aliasing energy [52]. Disjoint patterns were selected by minimizing both the aliasing energy for each pattern and the pair-wise correlation among patterns [32]. In Poisson sampling, a polynomial PDF was used to generate a random sampling pattern that maintains locally-uniform inter-sample distances. Disjoint patterns were generated by using a distinct starting seed for the sampling algorithm [93].

3.2.2 Profile-Encoding Reconstruction

In a recent study, we proposed to alleviate banding artifacts by combining separate CS reconstructions of individual phase-cycled bSSFP acquisitions [32]. The

individual-CS reconstruction (iCS) was implemented via a Lagrangian formulation:

$$\min_{m_n} \quad \|y_n - \mathcal{F}_{\mathcal{P}_n}\{m_n\}\|_2^2 + \lambda_1\|\psi\{m_n\}\|_1 + \lambda_2\|\nabla\{m_n\}\|_1 \tag{3.5}$$

This formulation comprised a data-consistency term (where y_n is the acquired data, $\mathcal{F}_{\mathcal{P}_n}$ is the partial Fourier operator, and m_n is the reconstructed image for the nth phase cycle), a sparsity term (where ψ is a wavelet-transform operator), and a total-variation term (TV; where ∇ is the finite difference operator). While iCS was shown to maintain good reconstruction quality for small N, loss of high-spatial-frequency information became prominent for N$\geq$4 due to increasingly heavier undersampling factors [32].

To address this limitation, we propose a profile-encoding bSSFP (PE-SSFP) reconstruction that solves the problem in Eq. 3.4 by synthesizing missing k-space samples from acquired data. First, an interpolation operator estimated from calibration data is used to iteratively synthesize nonacquired data across phase-cycles. Inspired by the SPIRiT model (iterative self-consistent parallel imaging) [93], the iterative estimation procedure enforces the consistency of reconstructed data with both the acquired and the calibration data. Lastly, PE-SSFP leverages joint sparsity [68, 9, 66] and TV penalties [4] to dampen aliasing and noise interference. Here PE-SSFP was implemented as a constrained optimization problem:

$$\begin{aligned} \min_{m} \quad & \lambda_1\left\|\sqrt{\sum_n |\psi\{m_n\}|^2}\right\|_1 + \lambda_2\sum_n \|\nabla\{m_n\}\|_1 \\ \text{subj. to} \quad & \|(\mathcal{G} - I)\{m\}\|_2^2 = 0 \\ & \sum_n \|y_n - \mathcal{F}_{\mathcal{P}_n}\{m_n\}\|_2^2 = 0 \end{aligned} \tag{3.6}$$

where m is the aggregate vector containing m_n across all phase-cycles. The objective comprises a joint sparsity term and a cumulative TV term across phase cycles. The first constraint enforces consistency of reconstructed data with the calibration data (where $\mathcal{G}$ is the aggregate interpolation operator, I is the identity operator). Meanwhile, the second constraint enforces cumulative data-consistency across phase cycles.

To efficiently solve the constrained optimization formulated in Eq. 3.6, we

leveraged an alternating projection-onto-sets scheme with the aim to produce a quasi-optimal solution at the intersection of multiple sets [66]. The optimization was split into four projection operators, namely calibration consistency, joint sparsity, TV, and data consistency projections. These projections were successively repeated to enforce relevant properties in the reconstructed data (see Fig. 3.2).

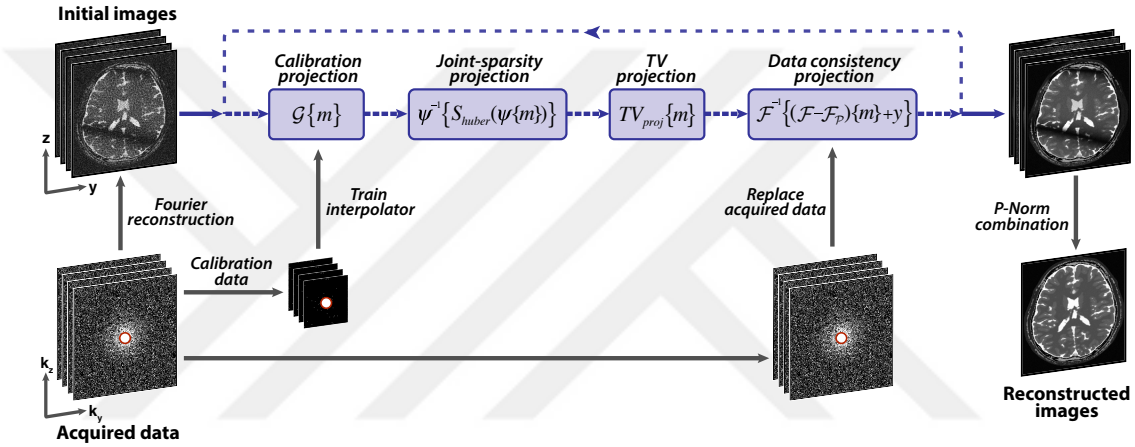

Figure 3.2: Flowchart of the profile-encoding bSSFP (PE-SSFP) reconstruction that recovers missing data in undersampled phase-cycled acquisitions. PE-SSFP employs an alternating projection-onto-sets scheme with four projection operators: calibration, joint-sparsity, TV, and data-consistency projections. In the calibration projection, an interpolation kernel estimated from calibration data is used to synthesize missing samples linearly from acquired data across phase-cycles. In the joint-sparsity projection, wavelet coefficients of phase-cycled bSSFP images are thresholded with a Huber function. In the TV projection, bSSFP images are denoised with a fast iterative-clipping algorithm. In the data-consistency projection, reconstructed data in sampled locations are replaced with their acquired values. These projections are successively repeated, and the individual phase-cycled images are finally combined with the p-norm method.

Calibration consistency: Prior to reconstruction, an interpolation kernel for profile encoding ($\mathcal{K}$) was obtained from aggregate calibration data y_{calib} (designated as the fully-sampled part of central k-space). Kernel weights that capture linear relationships among 11×11 neighborhoods of k-space samples were estimated based on the calibration constraint $(\mathcal{K} - I).y_{calib} = 0$. A 13×13 kernel was used at N=2 to leverage the relatively higher sampling density in central

k-space. The solution of this inverse problem was obtained via Tikhonov regularization (with weight $\alpha = 0.01$) to enhance noise resilience and conditioning [66]. Finally, an image-space operator $\mathcal{G}$ equivalent to the trained k-space kernel $\mathcal{K}$ was computed. During reconstruction, calibration-consistency projections were implemented by applying $\mathcal{G}$ on the image reconstructed in the previous iteration, $m^{(k)} = \mathcal{G}\left\{m^{(k-1)}\right\}$.

Joint sparsity: Assuming insignificant motion between separate acquisitions, tissue boundaries and sparsity patterns are expected to appear in identical locations across phase-cycled images. To leverage this correlated structural information, we utilized a joint-sparsity model that has been shown to offer benefits in other MR applications [68, 9, 93, 25, 100]. During PE-SSFP, the joint-sparsity term in Eq. 3.6 based on the Daubechies 4 wavelet can offer increased detection sensitivity for relatively small coefficients shared across phase cycles.

Wavelet-domain sparsity is conventionally enforced via shrinkage methods based on hard- $S_h(x) = \frac{x}{|x|-\lambda}.\max(0, |x| - \lambda)$ or soft-thresholding $S_s(x) = \frac{x}{|x|}.\max(0, |x| - \lambda)$, where λ is the threshold [101]. Both functions null wavelet coefficients below λ, potentially reducing detection sensitivity for small coefficients. To alleviate this issue, here we used a modified Huber function [102] :

$$S_{huber}(x) = \begin{cases} x^2/(2\lambda) & , |x| < \lambda \\ |x| - \lambda/2 & , \text{otherwise} \end{cases} \tag{3.7}$$

This function behaves similarly to soft-thresholding above λ, but it applies squared-weighting on small coefficients to increase detection sensitivity. Note that iterative thresholding based on this function provides a quasi-proximal mapping for the ℓ_1-norm, thus λ was set to λ_1 in Eq. 3.6. During PE-SSFP, the following joint-sparsity projections were applied: $m^{(\dot{k})} = \psi^{-1}\left\{S_{huber}(\psi\{m^{(k)}\})\right\}$.

TV: Total-variation projections were employed to reduce aliasing interference and noise. The projections were implemented by minimizing the objective $J(x) = \|m_n - x\|_2^2 + \lambda_2\|\nabla x\|_1$ using a fast iterative-clipping algorithm:

$$\begin{aligned} x^{(i)} &= m_n^{(\dot{k})} - \nabla^t z^{(i-1)} \\ z^{(i)} &= S_{clip}\left(z^{(i-1)} + \nabla x^{(i)}/\alpha\right) \end{aligned} \tag{3.8}$$

where ∇^t is the adjoint finite-difference operator, $z^{(1)} = 0$ and the update rate parameter $\alpha = 8$ [103]. The clipping function was modified to handle complex values:

$$S_{clip}(z) = \begin{cases} z & , |z| < \lambda_2/2 \\ (\lambda_2/2) \cdot exp(j\angle(z)) & , \text{otherwise} \end{cases} \tag{3.9}$$

where $\angle(z)$ is the phase of z. This algorithm converges rapidly, and the percentage change in the objective fell to 0.01% within 5 iterations during each TV projection: $m^{(\ddot{k})} = TV_{proj}\left\{m^{(\dot{k})}\right\}$.

Data consistency: To ensure consistency of reconstructed and acquired k-space data, reconstructed data were projected onto the constraint $\sum_n \|y_n - \mathcal{F}_{\mathcal{P}n}\{m_n\}\|_2^2 = 0$. This projection was implemented by replacing reconstructed data with the acquired data in sampled locations [66]: $m^{(\dddot{k})} = \mathcal{F}^{-1}\left\{(\mathcal{F} - \mathcal{F}_{\mathcal{P}})\{m^{(\ddot{k})}\} + y\right\}$.

The successive projections listed above were repeated until the percentage difference between the reconstructed images in consecutive iterations fell to 0.001%. Convergence was achieved within 15 iterations for the datasets considered here. The penalty weights $\lambda_{1,2}$ were varied separately in the range [0 10] $\times 10^{-3}$ with a step size of 10^{-3} for phantom data, and in the range [0 15] $\times 10^{-3}$ with a step size of 0.05×10^{-3} for in vivo data [52]. To minimize potential block artifacts and resolution losses, the smallest set of $\lambda_{1,2}$ that yielded satisfactory artifact/noise suppression were selected via visual inspection (see Table 3.1). To obtain a final bSSFP image, reconstructions for each phase-cycle were combined with the p-norm method (p=4), which was selected for its computational simplicity and favorable performance in artifact suppression and SNR efficiency [95].

Table 3.1: Regularization Parameters

	N = 2	**N = 4**	**N = 6**	**N = 8**
Brain (phantom)	8.0, 2.0	8.0, 2.0	8.0, 2.0	8.0, 2.0
Brain (in vivo)	1.5, 15	1.5, 15	0.75, 7.5	0.75, 7.5
Knee (in vivo)	0.15, 1.5	0.15, 1.5	0.075, 0.75	0.075, 0.75

Regularization parameters $\lambda_{1,2}(\times10^{-3})$ prescribed for PE-SSFP reconstructions are listed for each dataset and each N.

3.2.3 Alternative Reconstructions

To comparatively demonstrate PE-SSFP, zero-filled Fourier (ZF), individual CS (iCS) and ESPIRiT [104] reconstructions were also implemented. All methods reconstructed individual phase-cycled images that were then p-norm combined (p=4).

ZF: Nonacquired k-space data were filled with zeros. Data for each phase-cycle were compensated for the sampling density across k-space. An inverse Fourier transformation was then performed to reconstruct each phase-cycled image.

iCS: Individual CS reconstructions of phase-cycled acquisitions were implemented as described in Eq. 3.5. The sparsifying transform was selected as the Daubechies 4 wavelet. The optimization was performed using an iterative conjugate-gradient algorithm [4]. Iterations were repeated until the percentage difference between the reconstructed images in consecutive iterations fell to 0.01%. Convergence was achieved within 30 iterations for the datasets considered here. Further iterations were avoided because they were observed to cause undesirable blurring in the reconstructions. The regularization weights were scaled proportionately to those in PE-SSFP. Specifically, λ_1 was set to maintain the same ratio of sparsity to data-consistency terms ($\sqrt{N} \times \lambda_{1,PE-SSFP}$), λ_2 was set to maintain the same ratio of TV to data-consistency terms ($\lambda_{2,PE-SSFP}$).

ESPIRiT: A soft-SENSE reconstruction [94] based on multiple sets of bSSFP profiles was implemented using the ℓ_1-ESPIRiT framework [104]. Profile estimates were obtained via eigenvector decomposition of $\mathcal{G}$ in the image domain. Separate sets of profile estimates were obtained for each phase cycle ($\hat{C}_n^j$ for the j^{th} set, $j \in [1\ J]$), by selecting eigenvalues above a fixed threshold of 0.9 with a null-space cut-off σ^2_{cutoff}=0.02. This yielded two sets of bSSFP profiles estimates for the datasets reported here. Individual phase-cycled images m_n were then reconstructed via the following optimization:

$$\min_{m} \quad \sum_{n} \left\| y_n - \mathcal{F}_{\mathcal{P}_n} \{m_n\} \right\|_2^2 + \lambda_1 \left\| \sqrt{\sum_{n} |\psi\{m_n\}|^2} \right\|_1 \tag{3.10}$$

where $m_n = \sum_j \hat{C}_n^j m_n^j$. Variable splitting with a splitting parameter of 0.4 was implemented to decompose the optimization into two subproblems that minimize the profile-encoding cost (first term in the objective) and the joint-sparsity cost (second term) respectively [105]. The profile-encoding subproblem was solved via a conjugate gradient algorithm with 20 iterations [66]. Remaining reconstruction parameters including the number of outer iterations were kept identical to PE-SSFP.

3.2.4 Simulations

Simulations were performed based on a realistic brain phantom at 0.5 mm isotropic resolution (http://www.bic.mni.mcgill.ca/brainweb). Phase-cycled bSSFP signals for each tissue were calculated based on Eq. 3.1, assuming the following T_1/T_2: 3000/1000 ms for cerebro-spinal fluid (CSF), 1200/250 ms for blood, 1000/80 ms for white matter, 1300/110 ms for gray matter, 1400/30 ms for muscle, and 370/130 ms for fat. Meanwhile, three-dimensional (3D) acquisitions were simulated using $\alpha = 45^o$ (flip angle), TR = 5.0 ms, TE = 2.5 ms, 10 axial cross-sections equispaced to cover the whole brain in the superior-inferior direction, and $\Delta\phi = 2\pi\frac{[0:1:(N-1)]}{N}$. The simulations used a realistic field-inhomogeneity distribution corresponding to an off-resonance shift of 0±62 Hz (mean±std; see Fig. 3.1).

To demonstrate the auto-calibration approach used in PE-SSFP, we examined how well the acquired data can be represented via the bSSFP profiles estimated from calibration data. Using the profiles extracted by the ESPIRiT method [104], each phase-cycled image was projected onto the subspace spanned by the bSSFP profiles. A difference map was then calculated between each image and its projection onto this subspace. An aggregate error map was finally formed via sum-of-squares combination of difference maps across phase cycles. Error maps were generated for varying kernel sizes (5, 7, 9, 11, 13, 15, 17), calibration area sizes (6%, 8%, 10%, 12%, 14% of the maximum spatial frequency), and null-space cut-offs (σ^2_{cutoff}=2x$10^{-1,-2,-3,-4,-5}$).

Next, simulated brain images were undersampled by a factor of N in two phase-encode dimensions using patterns generated for uniform-density, variable-density, and Poisson disc sampling. Separate acquisitions were obtained for common and disjoint sampling patterns across phase cycles. PE-SSFP and alternative reconstructions were performed.

Reconstruction quality was assessed by several different metrics measured on combined bSSFP images. For a given cross-section, a mean-squared error (MSE) was first measured between the image reconstructed from N undersampled acquisitions and a reference image Fourier reconstructed from N=8 fully-sampled acquisitions. Because N=8 is typically sufficient for artifact suppression, MSE assessed the reconstruction performance in reducing banding artifacts in addition to aliasing/noise interference. The peak signal-to-noise (PSNR) metric was then derived from this MSE measurement to summarize the overall image quality. Lastly, a mean structural similarity index (SSIM) was measured between the reconstructed image and the reference image for N=8, following histogram matching to account for large-scale intensity variations [32]. SSIM assessed the degree of visual similarity in tissue structure to the reference image. To assess the reliability of PE-SSFP against field inhomogeneity, residual banding artifacts were evaluated on combined bSSFP images. CSF, white matter and gray matter signals were segregated via tissue masks. The level of residual artifact for each tissue was then characterized based on a percentage ripple metric. Ripple was taken as the ratio of the range of signal intensity to the mean intensity level. All metrics were pooled across 10 cross-sections in the phantom.

Several variants of PE-SSFP were implemented to assess the relative importance of the individual projection stages of the proposed method: PE_{calib} with only calibration and data-consistency projections; PE_{huber} with calibration, sparsity (based on Huber thresholding) and data-consistency projections; $\text{PE}_{soft-TV}$ with calibration, sparsity (based on soft thresholding), TV and data-consistency projections. Each additional projection included in PE-SSFP significantly improved the PSNR and SSIM values ($p<0.005$, signed-rank test). Furthermore, PE-SSFP outperformed that $\text{PE}_{soft-TV}$ for all $N>2$ ($p<0.005$). Thus, Huber thresholding was prescribed for all PE-SSFP reconstructions thereafter.

To examine the effect of tissue and sequence parameters on reconstruction performance, additional simulations were performed based on varying T_1/T_2 ratios, flip angles, TRs (with TE = TR/2), SNR levels, and acceleration factors (R). The following parameters were considered: (-40%, -20%, 0%, 20%, 40%) deviation in T_1/T_2 ratios, $\alpha = (15^o, 30^o, 45^o, 60^o, 75^o)$, TR = (5 ms, 10 ms, 15 ms), SNR levels ranging in [10 30] for CSF. To examine performance when R exceeds number of acquisitions (N), the following cases were simulated (N=2, R=4), (N=4, R=6), (N=4, R=8), and (N=6, R=8).

To evaluate noise performance, the SNR levels in the reconstructed images were compared against those in fully-sampled images. For this analysis, 30 separate noise instances with a bivariate Gaussian distribution were added to phase-cycled bSSFP images to attain acquisition SNR=20 for CSF. Each dataset was reconstructed to yield 30 separate combined bSSFP images. The SNR of each voxel was taken as the ratio of the mean to standard deviation of signal intensity across 30 images. A noise amplification map was then computed as the SNR ratio between the fully-sampled reference and reconstructed images. Significance of differences among reconstruction methods were assessed with nonparametric Wilcoxon signed-rank tests.

3.2.5 In Vivo Experiments

In vivo phase-cycled bSSFP images of the brain and the knee were collected on a 3 T Siemens Magnetom scanner (maximum gradient strength of 45 mT/m and slew rate of 200 T/m/s) with a 3D Cartesian sequence. The brain imaging protocol comprised a flip angle of 30^o, a TR/TE of 5.1/2.65 ms, a field-of-view (FOV) of 218 mm, an isotropic resolution of 0.85 mm, superior/inferior readout direction, N=8 separate acquisitions with phase-cycling values ($\Delta\phi$) spanning $[0, 2\pi)$ in equispaced intervals, and a 32-channel receive-only head coil. The knee imaging protocol comprised a flip angle of 30^o, a TR/TE of 5.0/2.5 ms, an FOV of 192 mm, an isotropic resolution of 1 mm, left/right readout direction, N=8, and a 15-channel receive-only knee coil. Fully-sampled images were combined across

coils to obtain single-channel multiple acquisition datasets. All participants gave written informed consent, and the imaging protocols were approved by the local ethics committee.

The brain and knee acquisitions were variable-density undersampled in the phase-encode dimensions to yield acceleration factors of 2-8, and profile-encoding reconstructions were performed. The following phase-cycling values were selected for reconstruction: $\Delta\phi = 2\pi\frac{[0:1:(N-1)]}{N}$ for N = 2, 4 and 8. The phase cycles for N = 6 were selected as a subset of those for N =8 (0, $\pi/2$, $3\pi/4$, π, $5\pi/4$, $7\pi/4$) to reduce overall scan time and minimize potential motion artifacts.

To examine the quality of reconstructed images, PSNR and SSIM metrics were measured across 10 equispaced cross-sections. For brain images, axial cross-sections were used that spanned across the entire volume in the superior-inferior direction. For knee images, sagittal cross-sections in the left-right direction were used. The reference image was taken as the combined Fourier reconstruction of N=8 fully-sampled acquisitions.

3.3 Results

3.3.1 Simulation Analyses

PE-SSFP was first demonstrated on bSSFP images of a numerical brain phantom. Figure 3.3 shows the combination bSSFP images reconstructed via ZF, iCS and PE-SSFP. As expected, heavier undersampling applied at higher N values increases aliasing interference in ZF images. Meanwhile iCS reconstructions, which process phase cycles independently, suffer from prominent losses in spatial resolution. In contrast, PE-SSFP successfully reduces aliasing interference while maintaining detailed tissue depiction even at N = 8.

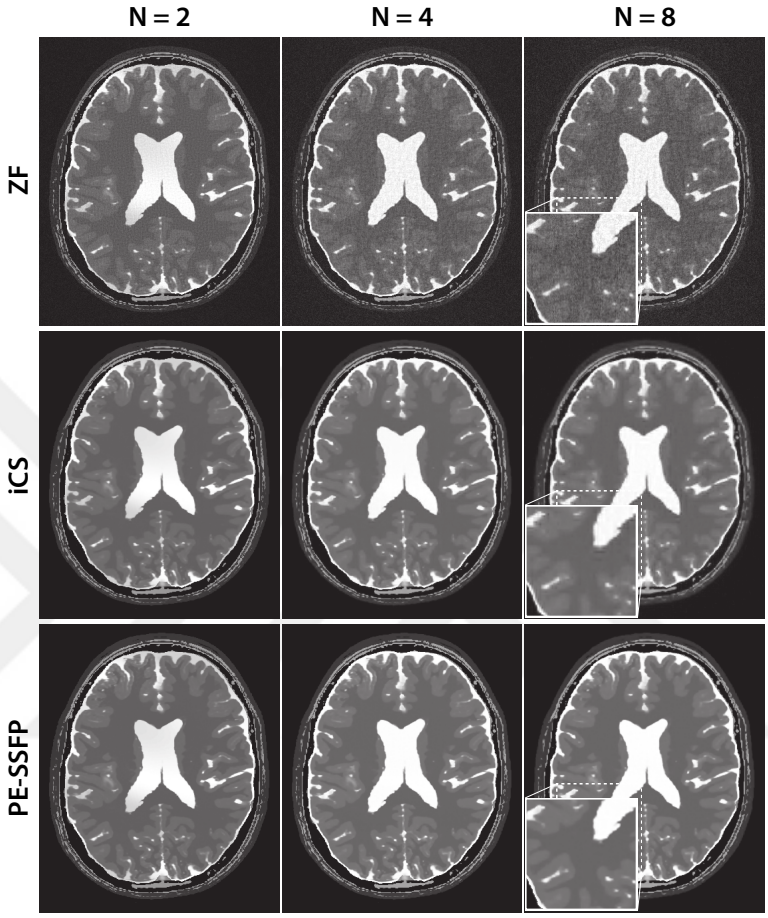

Figure 3.3: Phase-cycled bSSFP images of a numerical phantom were simulated for N=2-8, $\alpha = 45^o$, TR/TE=5.0/2.5 ms, a field map of 0±62 Hz (mean±std). Phantom images were undersampled by a factor of N via variable-density random sampling, disjointly across phase cycles. Zero-filled Fourier (ZF, top row), individual compressed sensing (iCS, middle row), and PE-SSFP (bottom row) reconstructions are shown. White boxes display a zoomed-in portion of the images. ZF reconstructions suffer from elevated aliasing/noise interference at high N due to the heavier undersampling factors used. While iCS reconstructions employ regularization terms that limit this interference, the heavy undersampling factors at high N cause visible loss of spatial resolution. In contrast, PE-SSFP successfully alleviates noise and aliasing interference while maintaining detailed depiction of tissue boundaries.

Several complementary analyses were performed to elucidate factors contributing to reconstruction performance. To demonstrate the auto-calibration approach in PE-SSFP, errors were examined in representing acquired data in terms of the bSSFP profiles estimated from calibration data. For the kernel size, calibration area and null-space cutoff prescribed in PE-SSFP, residual high-spatial-frequency errors occur near banding artifacts for each phase cycle. When combined across phase-cycles, the auto-calibration errors appear near tissue boundaries rather uniformly across the FOV. The average auto-calibration error relative to the maximum signal intensity is 3.2±0.6% (mean±s.e. across N). The percentage improvement that can be attained by advancing the kernel size, calibration area or null-space cutoff to their optimal values in the tested range is merely 1.0±0.3%. Thus, the selected PE-SSFP parameters yield near-optimal results with relatively low error levels. To determine the effects of individual projection operators in PE-SSFP, several variant reconstructions and respective squared-error maps relative to a fully-sampled image were computed (Fig. 3.4). The inclusion of each projection visibly reduces error across the image. To examine noise statistics of the reconstructions, noise amplification factors were calculated across the images (Fig. 3.5). Although the heavier undersampling at high N increases noise in ZF, penalty terms in iCS and PE-SSFP help maintain lower noise. In PE-SSFP, relatively higher amplification is observed near tissue boundaries that are more susceptible to resolution loss due to variable-density undersampling.

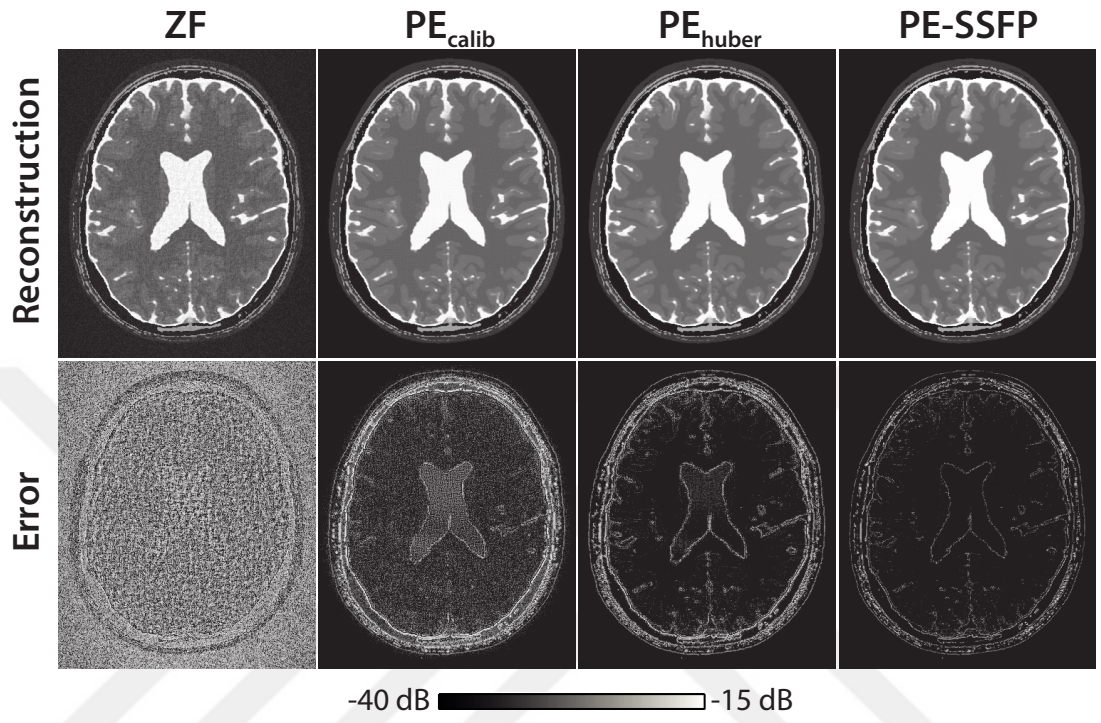

Figure 3.4: Representative bSSFP images of the numerical phantom for N=4 were reconstructed using ZF and PE-SSFP. Images from three variants of PE-SSFP are shown (top row). PE$_{calib}$ only uses calibration and data-consistency projections, PE$_{huber}$ uses calibration, joint-sparsity and data-consistency projections, and PE-SSFP additionally uses TV projections. Reconstructions were compared against a combination of fully-sampled images (for N=8). Squared-error maps are shown in logarithmic scale (bottom row; see colorbar). Each additional projection in PE-SSFP yields visibly reduced reconstruction error in bSSFP images.

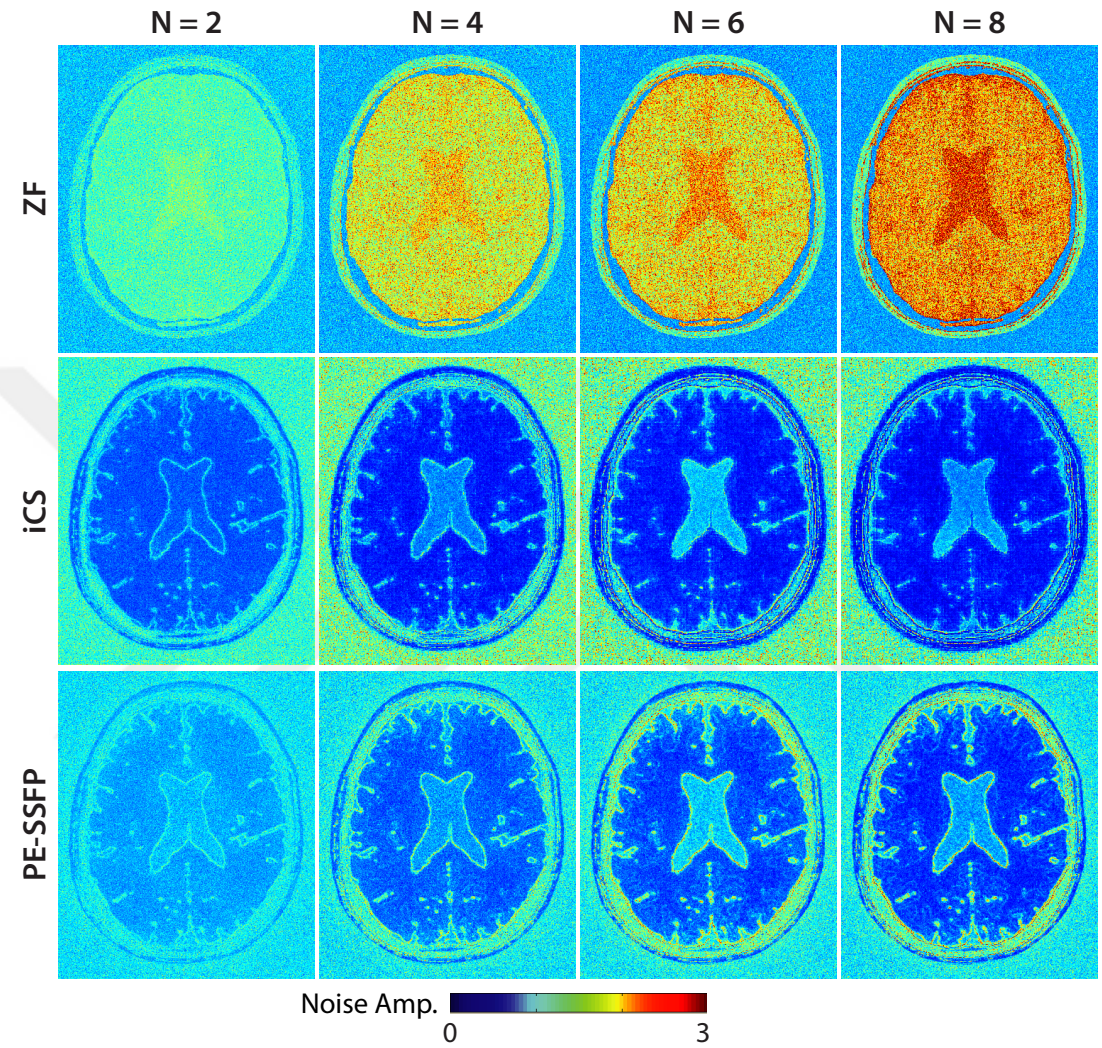

Figure 3.5: The noise-amplification maps for ZF, iCS and PE-SSFP methods are displayed for N=2-8. Although the heavier undersampling at high N increases noise amplification in ZF reconstructions, reconstructions with penalty terms iCS and PE-SSFP maintain relatively low noise amplification even at high N. The lower noise amplification with iCS likely reflects a bias from excessive loss of high-spatial-frequency information. In PE-SSFP, relatively higher amplification is observed near tissue boundaries that are more susceptible to resolution loss due to variable-density undersampling.

To determine the effect of the sampling strategy on PE-SSFP, uniform-density,

variable-density and Poisson disc undersampling patterns were tested. Each type of pattern was applied both commonly and disjointly across phase cycles. While all sampling strategies yield similar PSNR and SSIM values at N=2, variable-density (VD) disjoint sampling outperforms all other methods for N>2 ($p<0.005$). VD disjoint sampling improves PSNR by 4.0±1.9 dB (mean±s.e. across N) and SSIM by 0.8±0.5% over VD common sampling, and PSNR by 3.2±1.6 dB and SSIM by 0.4±0.2% over Poisson-disc disjoint sampling. Thus VD disjoint sampling was used for all reconstructions reported here.

Finally, PE-SSFP was comparatively evaluated against ZF, iCS and ESPIRiT. Representative images for N=8 are shown in Fig. 3.6 along with the squared-error maps in reference to a fully-sampled image. While ZF shows broadly distributed errors across the field-of-view, iCS reduces noise and aliasing interference at the expense of losses in high-spatial-frequency information. While ESPIRiT reconstructions alleviate this loss via joint-sparsity penalties, the respective images still show distributed errors. In contrast, PE-SSFP using both joint-sparsity and TV regularization effectively dampens the reconstruction errors in phase-cycled bSSFP images.

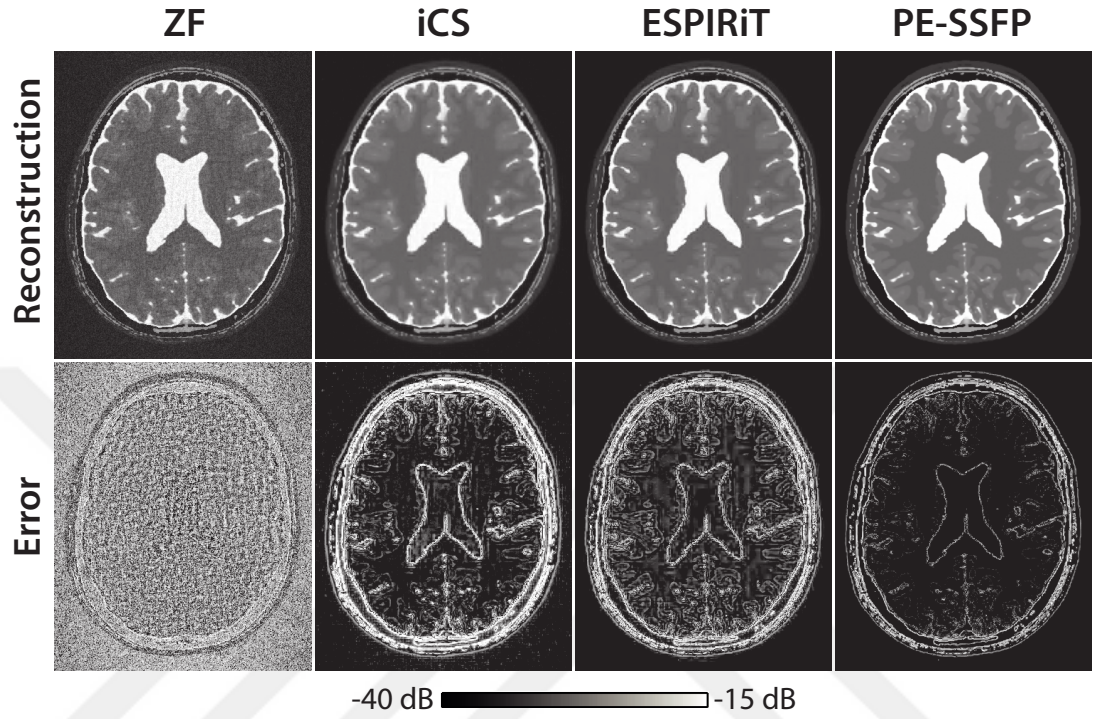

Figure 3.6: Phase-cycled bSSFP reconstructions of the numerical phantom (top row), and the squared-error maps with respect to the fully-sampled combination image (bottom row) are displayed for N=8. ZF has broadly distributed errors across the field-of-view due to aliasing and noise interference. iCS reconstructions reduce this interference via TV regularization at the expense of elevated errors near tissue boundaries, due to significant loss of high-spatial-frequency information. While ESPIRiT reconstructions alleviate this loss via joint-sparsity penalties, the respective images still show broadly distributed errors. In contrast, PE-SSFP using both joint-sparsity and TV regularization further dampens the reconstruction errors in phase-cycled bSSFP images.

The observations regarding PE-SSFP's superior image quality are supported by the quantitative assessments listed in Table 3.2. For each N, PE-SSFP yields significantly higher PSNR and SSIM values compared to all other reconstructions ($p<0.005$), with the exception of N=2 where iCS and PE-SSFP yield similar values. PE-SSFP improves PSNR by 13.1±5.0 dB and SSIM by 4.8±2.5% over iCS,

and PSNR by 14.5±3.2 dB and SSIM by 3.4±0.6% over ESPIRiT. The percentage ripple measurements listed in Table 3.2 indicate that PE-SSFP yields more homogeneous tissue signals compared to alternative methods for all N ($p<0.005$). Taken together, these results suggest that PE-SSFP reliably enhances image quality and artifact suppression compared to conventional reconstructions.

Table 3.2: Image Assessments for the Brain Phantom

Peak SNR and Structural Similarity

		N = 2	**N = 4**	**N = 6**	**N = 8**
ZF	PSNR	51.8±0.1	50.0±0.2	47.2±0.1	45.9±0.1
	SSIM	72.8±0.6	65.4±0.8	62.4±0.8	61.2±0.8
iCS	PSNR	57.5±0.5	61.3±0.3	52.3±0.4	49.0±0.3
	SSIM	97.9±0.1	97.0±0.0	91.4±0.3	88.2±0.3
ESPIRiT	PSNR	48.0±0.1	56.3±0.1	56.1±0.3	54.1±0.3
	SSIM	93.5±0.1	95.8±0.1	95.6±0.1	95.1±0.1
PE-SSFP	PSNR	57.9±0.4	78.2±0.3	71.5±0.4	64.9±0.3
	SSIM	98.4±0.1	98.8±0.0	98.4±0.0	98.0±0.0

Percentage Ripple

		N=2	**N=4**	**N=6**	**N=8**
ZF	CSF	38.8±2.1	29.7±1.6	31.9±2.1	32.5±2.1
	White	72.9±4.0	94.7±6.4	94.0±5.3	97.2±6.5
	Gray	53.8±2.1	73.2±5.1	76.3±3.2	77.8±5.5
iCS	CSF	23.2±0.8	8.9±1.1	17.9±1.4	23.9±2.6
	White	8.5±1.1	21.4±3.0	40.9±5.9	48.8±4.3
	Gray	9.7±1.1	17.7±1.4	30.8±4.6	36.7±6.2
ESPIRiT	CSF	43.9±1.1	17.5±2.1	18.8±1.5	19.7±1.4
	White	43.7±5.8	41.3±7.9	47.2±6.3	51.4±8.7
	Gray	39.0±3.8	28.7±2.7	34.5±3.8	36.1±5.0
PE-SSFP	CSF	22.5±0.2	2.1±0.2	3.4±0.5	3.1±0.5
	White	5.4±0.4	5.9±0.5	6.3±0.7	6.6±0.7
	Gray	8.3±0.3	6.9±0.4	6.8±0.4	7.4±1.1

Image assessment metrics measured in reconstructed bSSFP images of the numerical brain phantom. Metrics are reported separately for each reconstruction method as mean±std across 10 cross-sections. The top panel lists the peak SNR (PSNR) and structural similarity (SSIM) measurements obtained for $\alpha = 45^o$, TR = 5 ms, fixed T_1/T_2 values, and a realistic off-resonance frequency map (0±62 Hz). The bottom panel lists the percentage ripple measurements for CSF, white matter and gray matter separately.

3.3.2 In Vivo Analyses

PE-SSFP was demonstrated on bSSFP acquisitions of the brain and the knee. Similar to phantom results, the auto-calibration error was relatively low with 6.1±1.3% error (mean±s.e. across N) in the brain, and 3.7±0.7% error in the knee. Figure 3.7 shows the combined PE-SSFP images and the squared-error maps for N=2-8. As expected, prominent errors due to residual banding are visible for lower N values. These errors are alleviated towards high N, while maintaining high-quality tissue depiction. Representative images from ZF, iCS, ESPIRiT and PE-SSFP are displayed in Fig. 3.8. While iCS incurs losses at high spatial frequencies and coherent interference at low frequencies, ESPIRiT suffers from broadly distributed reconstruction errors across the images. In contrast, PE-SSFP visibly reduces reconstruction errors and preserves high-spatial-frequency information.

Quantitative assessments of in vivo reconstructions are listed in Table 3.3. In both the brain and the knee, PE-SSFP yields significantly higher PSNR and SSIM values compared to iCS for N>2 ($p<0.05$). PE-SSFP also improves PSNR and SSIM compared to all other alternative reconstructions for all N ($p<0.05$), with the exception of knee images at N=8 where PE-SSFP and ESPIRiT yield similar PSNR. In the brain, PE-SSFP improves PSNR by 3.0±2.6 dB and SSIM by 1.4±1.2% over iCS, and PSNR by 8.5±0.8 dB and SSIM by 7.1±0.5% over ESPIRiT. In the knee, PE-SSFP improves PSNR by 4.7±3.5 dB and SSIM by 1.8±0.6% over iCS, and PSNR by 2.8±1.2 dB and SSIM by 8.3±0.4% over ESPIRiT. Taken together, these results strongly suggest that the proposed method enables scan-efficient suppression of banding artifacts at high N values, while maintaining detailed tissue structure via the joint reconstruction.

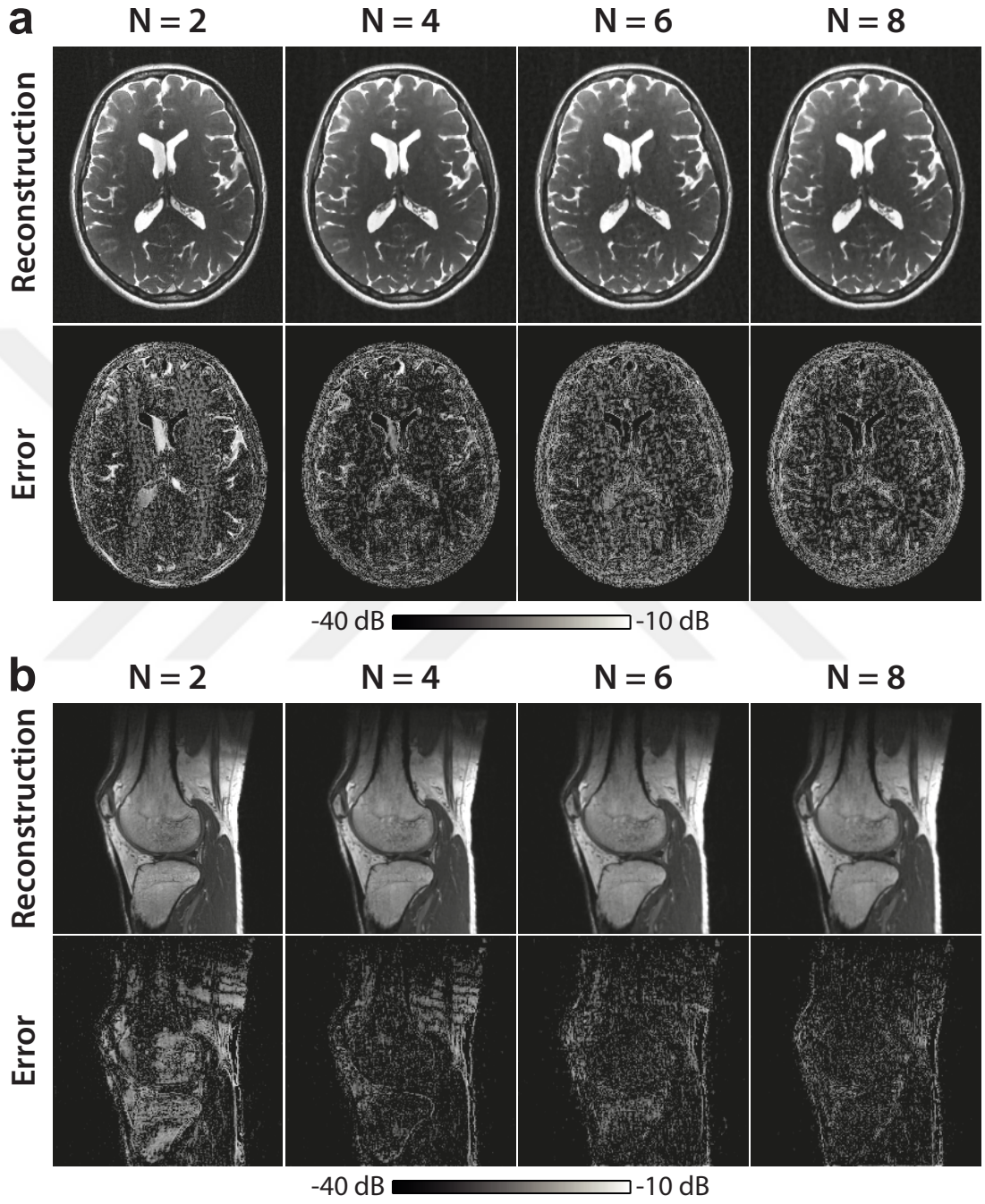

Figure 3.7: In vivo bSSFP acquisitions of the brain **(a)** and the knee **(b)** were reconstructed using PE-SSFP. Squared-error maps are shown in logarithmic scale (see colorbar). The error maps clearly suggest that banding artifact suppression improves for higher N, while PE-SSFP maintains detailed depiction of high-spatial-frequency information.

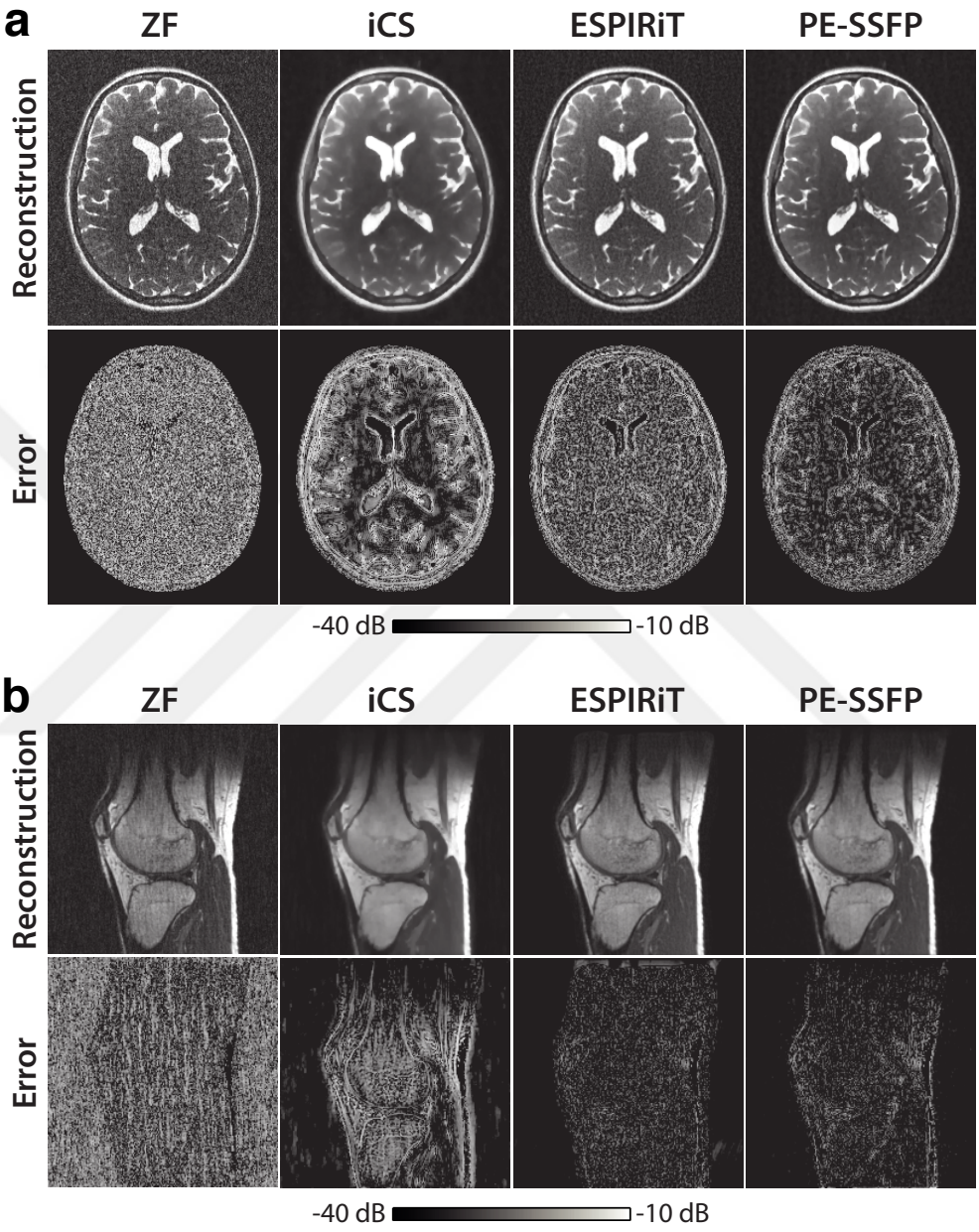

Figure 3.8: In vivo phase-cycled bSSFP reconstructions of the brain **(a)** and the knee **(b)** are displayed for N=8. ZF and ESPIRiT reconstructions suffer from broadly distributed reconstruction error across the images. Meanwhile, iCS reconstructions show substantial loss of high-spatial-frequency information and coherent low-frequency interference. In contrast, PE-SSFP effectively reduces errors due to aliasing and noise interference, while maintaining detailed tissue depiction.

Table 3.3: Image Assessments for In Vivo Datasets

Brain Images

		N=2	N=4	N=6	N=8
ZF	PSNR	48.6±0.2	44.1±0.4	41.4±0.4	40.3±0.4
	SSIM	73.5±0.6	56.4±0.8	50.6±0.7	48.9±0.8
iCS	PSNR	58.4±1.0	60.7±0.4	56.8±0.9	53.2±0.9
	SSIM	93.0±1.0	93.2±0.8	91.2±0.8	88.9±0.9
ESPIRiT	PSNR	49.5±0.5	53.4±0.4	51.8±0.6	52.5±0.5
	SSIM	84.2±0.7	87.6±0.8	84.7±0.5	86.7±0.7
PE-SSFP	PSNR	56.0±0.7	62.5±0.5	61.0±0.8	61.5±0.7
	SSIM	92.0±0.5	94.0±0.4	92.7±0.4	93.0±0.3

Knee Images

		N = 2	N = 4	N = 6	N = 8
ZF	PSNR	59.6±0.3	57.8±0.5	55.7±0.3	54.4±0.4
	SSIM	86.2±0.6	77.2±0.9	72.8±1.1	69.2±1.1
iCS	PSNR	65.2±0.7	72.8±0.4	65.3±0.9	63.0±1.2
	SSIM	94.7±0.5	95.5±0.4	92.0±0.4	90.5±0.2
ESPIRiT	PSNR	60.5±0.4	68.3±0.4	70.7±0.6	74.6±0.6
	SSIM	84.5±1.2	87.2±2.4	87.2±2.4	87.8±2.3
PE-SSFP	PSNR	63.9±0.5	73.3±0.4	73.4±0.7	74.5±0.6
	SSIM	93.5±0.4	95.8±0.2	95.2±0.3	95.4±0.3

Image assessment metrics measured in reconstructed bSSFP images of in vivo brain and knee data. Metrics are reported separately for each reconstruction method as mean±std across 10 cross-sections. The top panel lists PSNR and SSIM measurements for brain images, and the bottom panel lists the measurements for knee images.

3.4 Discussion

Here we evaluted an improved acceleration framework for multiple-acquisition 3D bSSFP based on variable-density random undersampling in two phase-encode dimensions. In this framework, nonacquired data across phase-cycles are simultaneously synthesized using a profile-encoding reconstruction that enforces joint sparsity and TV penalties. A p-norm combination of individual phase-cycled images yields a final artifact-suppressed bSSFP image.

Several alternative approaches were previously proposed for reducing banding artifacts. One strategy is to increase the tolerable range of field inhomogeneity by modifying the bSSFP magnetization profile [80, 81, 82, 83]. Alternatively, advanced shimming procedures can be performed to directly limit field inhomogeneity [84]. While both strategies aim to reduce banding artifacts during acquisition, they require complex pulse-sequence modifications and prolonged scan times. In contrast, our proposed framework can be implemented via standard bSSFP sequences without separate calibration procedures.

Improvements in scan efficiency of multiple-acquisition bSSFP have been considered in several previous reports. Recently, we proposed to undersample and individually reconstruct phase-cycled acquisitions using CS [32]. The CS framework yielded high quality reconstructions up to an acceleration factor of N=4. Another study employed simultaneous multislice imaging to accelerate each acquisition separately, and similarly considered N$\leq$4 [92]. While these previous studies disregarded image features shared across phase-cycles, here we used a joint-sparsity model to enhance recovery of wavelet coefficients, and TV regularization to reduce aliasing and noise interference. Due to these advances, PE-SSFP maintains high-quality reconstructions up to N=8. Spatial encoding by coil arrays was not leveraged in the reconstructions reported here. However, if more effective artifact suppression is needed (e.g., while imaging at 7T or near air-tissue interfaces), a higher N value and a respectively higher acceleration factor might be maintained by also leveraging coil sensitivity information. Note, however, that each phase-cycled acquisition involves a fixed-duration overhead due

to the preparatory RF pulses employed to reach steady state. This overhead will become more prominent for larger N values, reducing the overall scan efficiency.

With similar motivations to PE-SSFP, one earlier study proposed a SENSE-type reconstruction performed jointly across phase-cycled acquisitions, each accelerated via uniform-density undersampling [96]. Sensitivity estimates were taken as the ratio of low resolution phase-cycled images to a maximum-intensity combination of these images. In contrast, here we used variable-density sampling, and we did not assume any combination model while calibrating the interpolation kernel. Our results clearly indicate that variable-density sampling offers improved performance compared to uniform sampling.

PE-SSFP can be potentially improved by addressing several limitations. First, if significant motion occurs in between separate acquisitions, image structure can be displaced across phase-cycles. These displacements may in turn violate the joint-sparsity model and yield suboptimal reconstructions. A motion-correction operator could be incorporated to alleviate motion-induced performance loss. Second, the auto-calibration approach in PE-SSFP relies on the assumption that bSSFP spatial profiles vary gradually. Rapid profile variations near tissue boundaries or bSSFP nulls can yield suboptimal interpolation operators, increasing reconstruction errors. This issue may be of particular concern with high field strengths, long TRs, and certain combinations of T_1/T_2 and flip angles. In such cases, the k-space calibration area could be expanded and interpolation kernels of variable widths across k-space could be used to improve accuracy of the interpolation operator [106, 107]. Third, while a p-norm combination was observed to yield good artifact suppression in this study, it could be replaced with sophisticated techniques that leverage analytical signal models to further improve artifact suppression [85, 86]. Lastly, optimization with the projection-onto-sets method does not guarantee convergence onto a fixed solution in the absence of overlap between the projection sets. While we observed good convergence behavior here, reconstruction stability can be improved by modern approaches such as the alternating direction method of multipliers [108].

In conclusion, the proposed PE-SSFP framework jointly reconstructs multiple-acquisition bSSFP data by leveraging shared sparsity patterns across phase-cycles. PE-SSFP was primarily demonstrated for brain and knee imaging in the current study. Nonetheless, the scan-efficient acquisitions and high-quality reconstructions enabled by PE-SSFP could improve other multiple-acquisition bSSFP applications such as peripheral angiography [14], coronary imaging [109], and fat/water separation [110, 90].

Chapter 4

Conclusion

In this chapter, we provide a summary of the work presented in the thesis, and discuss the future research. This thesis deals with the development and application of two image reconstruction frameworks for accelerated acquisitions. These frameworks are based on compressed sensing reconstructions of magnetic resonance angiography and balanced steady-state free precession imaging. In Chapter 2, we demonstrated that a two-step reconstruction strategy with adaptive regularization weights can improve the performance of compressed sensing reconstructions compared to conventional methods. Our results indicate that adaptive reconstruction scheme can increase the clinical potential of both compressed sensing reconstructions and non-contrast enhanced angiography methods. In Chapter 3, we demonstrated an improved framework for multiple-acquisition bSSFP acquisitions. By leveraging shared sparsity patterns across phase-cycles, we were able to obtain an artifact-free images within the total scan time equivalent to a single acquisition. Extensive simulations and in vivo experiments demonstrated the improvements achieved with the developed framework, further increasing the potential usefulness of bSSFP sequences in clinical and research applications.

4.1 Future Work

Based on these results, there are a number of interesting research directions to be targeted in the future. One of the critical limitations of compressed sensing reconstructions for the clinical implementation is selecting appropriate regularization parameters in the reconstruction. For the best diagnostic image quality, compressed sensing algorithms usually require hand-tuning of these regularization parameters, which is tedious task and impractical for clinical utilization [2, 111]. Using low regularization parameters may result in insufficient suppression of aliasing artifacts and noise interference, whereas using excessive terms can lead to removal of important image features for clinical evaluation [3]. Although recent works have tried to address this problem, the accuracy and radiological assessments of these methods remains an open problem [112, 113, 114, 115].

Another critical requirement for the clinical implementation of compressed sensing reconstructions is the computation time. Delays between the acquisition and visualization of data represents a great challenge for the clinical use of CS [2]. Many researchers have focused their attention on parallel implementations on graphics hardware [69, 66, 116] and web-based cloud computational systems [117] for faster reconstruction times. However, the increase of receiver coil channels and demand for higher resolution images require further speed-ups in computation time and this gives rise to an important direction for future studies.

4.2 Contributions to the Literature

4.2.1 Journal Papers

[1] E. Ilicak, S. Cetin, E. Bulut, K. Oguz, E. Saritas, G. Unal, and T. Çukur, 'Targeted vessel reconstruction in non-contrast-enhanced steady-state free precession angiography.,' NMR in biomedicine, vol. 29, no. 5, pp. 53244, 2016.

[2] E. Ilicak, L. Senel, E. Biyik, and T. Çukur, 'Profile-encoding reconstruction for multiple-acquisition balanced steady-state free precession imaging.,' Magnetic resonance in medicine, 2016.

4.2.2 Conference Papers

[1] E. Ilicak, S. Cetin, E. U. Saritas, G. Unal and T. Çukur, 'Adaptive reconstruction for vessel preservation in unenhanced MR angiography,' 2016 24th Signal Processing and Communication Application Conference (SIU), Zonguldak, 2016, pp. 577-580.

[2] E. Ilicak, and T. Çukur, 'Parameter-Free Profile Encoding Reconstruction for Multiple-Acquisition BSSFP Imaging,' In Proceedings of the 25th Annual Meeting of ISMRM, (Honoululu), p. 571, 2017.

[3] T. Kilic, E. Ilicak, T. Çukur, and E. Saritas 'Improved SPIRiT Operator for Joint Reconstruction of Multiple T2-Weighted Images,' In Proceedings of the 25th Annual Meeting of ISMRM, (Honoululu), p. 5165, 2017.

[4] Y. Can, E. Ilicak, and T. Çukur, 'Fast 3D Variable-FOV Reconstruction for Parallel Imaging with Localized Sensitivities,' In Proceedings of the 25th Annual Meeting of ISMRM, (Honoululu), p. 5158, 2017.

4.2.3 Additional Contributions

[1] Y. Can, E. Ilicak, and T. Çukur, 'Fast 3D Variable-FOV Reconstruction for Parallel Imaging with Localized Sensitivities,' arXiv preprint arXiv:1612.00157, 2016.

[2] E. Byk, E. Ilicak, and T. Çukur, 'Reconstruction by Calibration over Tensors for Multi-Coil Multi-Acquisition Balanced SSFP Imaging,' arXiv preprint arXiv:1704.00096, 2017.

Bibliography

[1] D. Nishimura, "Principles of magnetic resonance imaging." Stanford University EE369B Course Notes, 1996.

[2] O. N. Jaspan, R. Fleysher, and M. L. Lipton, "Compressed sensing MRI: a review of the clinical literature.," *Br J Radiology*, vol. 88, no. 1056, p. 20150487, 2015.

[3] L. Feng, T. Benkert, K. Block, D. K. Sodickson, R. Otazo, and H. Chandarana, "Compressed sensing for body MRI," *J Magn Reson Imaging*, vol. 45, no. 4, pp. 966–987, 2017.

[4] M. Lustig, D. Donoho, and J. M. Pauly, "Sparse MRI: The application of compressed sensing for rapid MR imaging.," *Magn Reson Med*, vol. 58, pp. 1182–1195, Dec. 2007.

[5] M. A. Bernstein, K. F. King, and X. J. Zhou, *Handbook of MRI pulse sequences*. Burlington, MA: Elsevier Academic Press, 1st ed., 2004.

[6] M. Loecher and O. Wieben, *k-Space*, pp. 13–23. Cham: Springer International Publishing, 2015.

[7] M. Lustig, D. L. Donoho, J. M. Santos, and J. M. Pauly, "Compressed sensing mri," *IEEE Signal Processing Magazine*, vol. 25, pp. 72–82, March 2008.

[8] T. Çukur, M. Lustig, and D. G. Nishimura, "Improving non-contrast-enhanced steady-state free precession angiography with compressed sensing," *Magn Reson Med*, vol. 61, no. 5, pp. 1122–1131, 2009.

[9] R. Otazo, D. Kim, L. Axel, and D. K. Sodickson, "Combination of compressed sensing and parallel imaging for highly accelerated first-pass cardiac perfusion MRI.," *Magn Reson Med*, vol. 64, pp. 767–776, Sept. 2010.

[10] F. R. Korosec, *Basic Principles of MRI and MR Angiography*, pp. 3–38. New York, NY: Springer New York, 2012.

[11] T. J. Fraum, D. R. Ludwig, M. R. Bashir, and K. J. Fowler, "Gadolinium-based contrast agents: A comprehensive risk assessment," *J Magn Reson Imaging*, 2017.

[12] H. Zhang, W. Zhang, and M. R. Prince, *Technical Aspect of Contrast-Enhanced MRA*, pp. 65–73. New York, NY: Springer New York, 2012.

[13] S. Yu, L. Yan, Y. Yao, S. Wang, M. Yang, B. Wang, Y. Zhuo, L. Ai, X. Miao, and J. Zhao, "Noncontrast dynamic MRA in intracranial arteriovenous malformation (AVM): comparison with time of flight (TOF) and digital subtraction angiography (DSA)," vol. 30, no. 6, pp. 869–877, 2012.

[14] T. Çukur, J. H. Lee, N. K. Bangerter, B. A. Hargreaves, and D. G. Nishimura, "Non-contrast-enhanced flow-independent peripheral MR angiography with balanced SSFP," *Magn Reson Med*, vol. 61, no. 6, pp. 1533–1539, 2009.

[15] I. Koktzoglou, R. P. Lim, O. Flanagan, and R. R. Edelman, *Non-contrast Enhanced MRA*, pp. 297–314. Cham: Springer International Publishing, 2015.

[16] M. Miyazaki and H. Isoda, "Non-contrast-enhanced MR angiography of the abdomen," *European journal of radiology*, 2011.

[17] M. P. Hartung, T. M. Grist, and C. J. François, "Magnetic resonance angiography: current status and future directions," *Journal of Cardiovascular Magnetic Resonance*, vol. 13, p. 19, Mar 2011.

[18] Y. Amano, K. Takahama, and S. Kumita, "Non-contrast-enhanced MR angiography of the thoracic aorta using cardiac and navigator-gated magnetizationprepared three-dimensional steady-state free precession," *J Magn Reson Imaging*, vol. 27, no. 3, pp. 504–509, 2008.

[19] S. W. Fielden, J. P. Mugler, K. D. Hagspiel, P. T. Norton, C. M. Kramer, and C. H. Meyer, "Noncontrast peripheral MRA with spiral echo train imaging," *Magn Reson Med*, vol. 73, no. 3, pp. 1026–1033, 2015.

[20] J. D. Trzasko, C. R. Haider, E. A. Borisch, N. G. Campeau, J. F. Glockner, S. J. Riederer, and A. Manduca, "Sparse-CAPR: highly accelerated 4D CE-MRA with parallel imaging and nonconvex compressive sensing.," *Magn Reson Med*, vol. 66, pp. 1019–1032, Oct. 2011.

[21] D. C. Peters, F. R. Korosec, T. M. Grist, W. F. Block, J. E. Holden, K. K. Vigen, and C. A. Mistretta, "Undersampled projection reconstruction applied to MR angiography," *Magn Reson Med*, vol. 43, no. 1, pp. 91–101, 2000.

[22] H. H. Hu, A. J. Madhuranthakam, D. G. Kruger, J. Huston, and S. J. Riederer, "Improved venous suppression and spatial resolution with sense in elliptical centric 3d contrast-enhanced mr angiography," *Magnetic Resonance in Medicine*, vol. 52, no. 4, pp. 761–765, 2004.

[23] P. M. Mostardi, J. F. Glockner, P. M. Young, and S. J. Riederer, "Contrast-enhanced mr angiography of the abdomen with highly accelerated acquisition techniques," *Radiology*, vol. 261, no. 2, pp. 587–597, 2011. PMID: 21900616.

[24] J. Trzasko, C. Haider, and A. Manduca, "Practical nonconvex compressive sensing reconstruction of highly-accelerated 3d parallel mr angiograms," in *2009 IEEE International Symposium on Biomedical Imaging: From Nano to Macro*, pp. 274–277, June 2009.

[25] M. Akçakaya, P. Hu, M. L. Chuang, T. H. Hauser, L. H. Ngo, W. J. Manning, V. Tarokh, and R. Nezafat, "Accelerated noncontrast-enhanced pulmonary vein MRA with distributed compressed sensing.," *J Magn Reson Imaging*, vol. 33, pp. 1248–1255, May 2011.

[26] H. Y. Carr, "Steady-state free precession in nuclear magnetic resonance," *Phys Rev*, vol. 112, pp. 1693–1701, 1958.

[27] O. Bieri and K. Scheffler, "Fundamentals of balanced steady state free precession MRI," *J Magn Reson Imaging*, vol. 38, no. 1, pp. 2–11, 2013.

[28] B. A. Hargreaves, G. E. Gold, C. F. Beaulieu, S. S. Vasanawala, D. G. Nishimura, and J. M. Pauly, "Comparison of new methods for magnetic resonance imaging of articular cartilage," *Magn Reson Med*, vol. 49, no. 4, pp. 700–709, 2003.

[29] T. Çukur, N. K. Bangerter, and D. G. Nishimura, "Enhanced spectral shaping in steady-state free precession imaging," *Magn Reson Med*, vol. 58, pp. 1216–1223, 2007.

[30] S. S. Vasanawala, B. A. Hargreaves, J. M. Pauly, D. G. Nishimura, C. F. Beaulieu, and G. E. Gold, "Rapid musculoskeletal MRI with phase-sensitive steady-state free precession: Comparison with routine knee MRI," *AJR Am J Roentgenol*, vol. 184, pp. 1450–1455, 2004.

[31] T. Çukur and D. G. Nishimura, "Multiple repetition time balanced steady–state free precession imaging.," *Magn Reson Med*, vol. 62, pp. 193–204, July 2009.

[32] T. Cukur, "Accelerated Phase-Cycled SSFP Imaging With Compressed Sensing," *Medical Imaging, IEEE Transactions on*, vol. 34, pp. 107–115, Jan. 2015.

[33] Y. Zur, M. L. Wood, and L. J. Neuringer, "Motion-insensitive, steady-state free precession imaging," *Magn Reson Med*, vol. 16, no. 3, pp. 444–459, 1990.

[34] P. Marckmann, L. Skov, K. Rossen, A. Dupont, M. B. Damholt, J. G. Heaf, and H. S. Thomsen, "Nephrogenic systemic fibrosis: suspected causative role of gadodiamide used for contrast-enhanced magnetic resonance imaging," *J Am Soc Nephrol*, vol. 17, no. 9, pp. 2359–2362, 2006.

[35] M. Miyazaki and V. S. Lee, "Nonenhanced MR angiography," *Radiology*, vol. 248, pp. 20–43, 2008.

[36] N. K. Bangerter, T. Cukur, B. A. Hargreaves, B. S. Hu, J. H. Brittain, D. Park, G. E. Gold, and D. G. Nishimura, "Three-dimensional fluid-suppressed T2-prep flow-independent peripheral angiography using balanced SSFP.," *Magn Reson Imaging*, vol. 29, pp. 1119–1124, Oct. 2011.

[37] T. Çukur, A. Shimakawa, H. Yu, B. A. Hargreaves, B. S. Hu, D. G. Nishimura, and J. H. Brittain, "Magnetization-prepared IDEAL bSSFP: A flow-independent technique for noncontrast-enhanced peripheral angiography.," *J Magn Reson Imaging*, vol. 33, pp. 931–939, Apr. 2011.

[38] H. Wu, W. F. Block, and A. A. Samsonov, "HYPR-Constrained Compressed Sensing Reconstruction for Accelerated Time Resolved Imaging," in *Proceedings of the 16th Annual Meeting of ISMRM*, (Toronto), p. 339, 2008.

[39] K. T. Block, M. Uecker, and J. Frahm, "Undersampled radial MRI with multiple coils: Iterative image reconstruction using a total variation constraint," *Magn Reson Med*, vol. 57, pp. 1086–1098, 2007.

[40] U. Gamper, P. Boesiger, and S. Kozerke, "Compressed sensing in dynamic MRI," *Magn Reson Med*, vol. 59, no. 2, pp. 365–373, 2008.

[41] J. P. Haldar, D. Hernando, S. Song, and Z. Liang, "Anatomically constrained reconstruction from noisy data.," *Magn Reson Med*, vol. 59, pp. 810–818, Apr. 2008.

[42] E. Gong, F. Huang, K. Ying, W. Wu, S. Wang, and C. Yuan, "PROMISE: parallel-imaging and compressed-sensing reconstruction of multicontrast imaging using SharablE information.," *Magn Reson Med*, vol. 73, pp. 523–535, Feb. 2015.

[43] D. Liang, E. V. R. DiBella, R.-R. Chen, and L. Ying, "k-t ISD: dynamic cardiac MR imaging using compressed sensing with iterative support detection.," *Magn Reson Med*, vol. 68, pp. 41–53, July 2012.

[44] K. M. Johnson, J. Velikina, Y. Wu, S. Kecskemeti, O. Wieben, and C. A. Mistretta, "Improved waveform fidelity using local HYPR reconstruction (HYPR LR).," *Magn Reson Med*, vol. 59, pp. 456–462, Mar. 2008.

[45] E. G. Stinson, E. A. Borisch, C. P. Johnson, J. D. Trzasko, P. M. Young, and S. J. Riederer, "Vascular masking for improved unfolding in 2D SENSE-accelerated 3D contrast-enhanced MR angiography.," *J Magn Reson Imaging*, vol. 39, pp. 1161–1170, May 2014.

[46] H. Oh and S. Lee, "Visually weighted reconstruction of compressive sensing MRI.," *Magn Reson Imaging*, vol. 32, pp. 270–280, Apr. 2014.

[47] C. Zhang, M. van de Giessen, E. Eisemann, and A. Vilanova, "User-guided compressed sensing for magnetic resonance angiography," in *Engineering in Medicine and Biology Society (EMBC), 2014 36th Annual International Conference of the IEEE*, pp. 2416–2419, 2014.

[48] A. S. Konar, S. Aiholli, H. C. Shashikala, D. R. Ramesh Babu, and S. Geethanath, "Application of Region of Interest Compressed Sensing to accelerate magnetic resonance angiography.," *Conf Proc IEEE Eng Med Biol Soc*, vol. 2014, pp. 2428–2431, Aug. 2014.

[49] J. Hutter, R. Grimm, C. Forman, J. Hornegger, and P. Schmitt, "Vessel Adapted Regularization for Iterative Reconstruction in MR Angiography," in *Proc 20th Annual Meeting of Int Soc Magn Reson Med*, p. 2541, 2012.

[50] S. Cetin and G. Unal, "A Higher-Order Tensor Vessel Tractography for Segmentation of Vascular Structures.," *IEEE Trans Med Imaging*, vol. 34, pp. 2172–2185, Oct. 2015.

[51] B. A. Hargreaves, S. S. Vasanawala, J. M. Pauly, and D. G. Nishimura, "Characterization and reduction of the transient response in steady-state MR imaging," *Magn Reson Med*, vol. 46, no. 1, pp. 149–158, 2001.

[52] T. Çukur, M. Lustig, E. U. Saritas, and D. G. Nishimura, "Signal Compensation and Compressed Sensing for Magnetization-Prepared MR Angiography.," *IEEE Trans Med Imaging*, vol. 34, pp. 107–115, Jan. 2011.

[53] R. M. Stefancik and M. Sonka, "Highly automated segmentation of arterial and venous trees from three-dimensional magnetic resonance angiography (MRA).," *Int J Cardiovasc Imaging*, vol. 17, pp. 37–47, Feb. 2001.

[54] X. Tizon and O. Smedby, "Segmentation with gray-scale connectedness can separate arteries and veins in MRA.," *J Magn Reson Imaging*, vol. 15, pp. 438–445, Apr. 2002.

[55] B. E. Chapman, J. O. Stapelton, and D. L. Parker, "Intracranial vessel segmentation from time-of-flight MRA using pre-processing of the MIP Z-buffer: accuracy of the ZBS algorithm.," *Med Image Anal*, vol. 8, pp. 113–126, June 2004.

[56] P. J. H. de Koning, J. A. Schaap, J. P. Janssen, J. J. M. Westenberg, R. J. van der Geest, and J. H. C. Reiber, "Automated segmentation and analysis of vascular structures in magnetic resonance angiographic images," *Magn Reson Med*, vol. 50, pp. 1189–1198, Nov. 2003.

[57] M. Müller-Eschner, T. Müller, A. Biesdorf, S. Wörz, F. Rengier, D. Böckler, H.-U. Kauczor, K. Rohr, and H. von Tengg-Kobligk, "3D morphometry using automated aortic segmentation in native MR angiography: an alternative to contrast enhanced MRA?," *Cardiovasc Diagn Ther*, vol. 4, pp. 80–87, Apr. 2014.

[58] S. Cetin, A. Demir, A. Yezzi, M. Degertekin, and G. Unal, "Vessel tractography using an intensity based tensor model with branch detection.," *IEEE Trans Med Imaging*, vol. 32, pp. 348–363, Feb. 2013.

[59] S. Cetin and G. Unal, "Higher order tensor-based segmentation and n-furcation modeling of vascular structures," in *Proceedings of the Joint MICCAI Workshop CVII STENT*, (Boston), p. 68, 2014.

[60] E. Yip, J. Yun, K. Wachowicz, A. A. Heikal, Z. Gabos, S. Rathee, and B. G. Fallone, "Prior data assisted compressed sensing: A novel MR imaging strategy for real time tracking of lung tumors.," *Med Phys*, vol. 41, p. 082301, Aug. 2014.

[61] J. C. Ye, S. Tak, Y. Han, and H. W. Park, "Projection reconstruction MR imaging using FOCUSS.," *Magn Reson Med*, vol. 57, pp. 764–775, Apr. 2007.

[62] R. L. Greenman, J. E. Shirosky, R. V. Mulkern, and N. M. Rofsky, "Double inversion black-blood fast spin-echo imaging of the human heart: A comparison between 1.5T and 3.0T," *J Magn Reson Imaging*, vol. 17, pp. 648–655, 2003.

[63] B. I. Mazhbich, "Noninvasive determination of elastic properties and diameter of human limb arteries.," *Pflugers Arch*, vol. 396, no. 3, pp. 254–259, 1983.

[64] C. D. Constantinides, E. Atalar, and E. R. McVeigh, "Signal-to-noise measurements in magnitude images from NMR phased arrays," *Magn Reson Med*, vol. 38, no. 5, pp. 852–857, 1997.

[65] Q. Zhang, R. Plemmons, D. Kittle, D. Brady, and S. Prasad, "Joint segmentation and reconstruction of hyperspectral data with compressed measurements.," *Appl Opt*, vol. 50, pp. 4417–4435, Aug. 2011.

[66] M. Murphy, M. Alley, J. Demmel, K. Keutzer, S. Vasanawala, and M. Lustig, "Fast ℓ_1-SPIRiT compressed sensing parallel imaging MRI: scalable parallel implementation and clinically feasible runtime.," *IEEE Trans Med Imaging*, vol. 31, pp. 1250–1262, June 2012.

[67] S. Nam, M. Akçakaya, T. Basha, C. Stehning, W. J. Manning, V. Tarokh, and R. Nezafat, "Compressed sensing reconstruction for whole-heart imaging with 3D radial trajectories: a graphics processing unit implementation.," *Magn Reson Med*, vol. 69, pp. 91–102, Jan. 2013.

[68] D. Liang, B. Liu, J. Wang, and L. Ying, "Accelerating SENSE using compressed sensing," *Magn Reson Med*, vol. 62, no. 6, pp. 1574–1584, 2009.

[69] F. Knoll, K. Bredies, T. Pock, and R. Stollberger, "Second order total generalized variation (TGV) for MRI.," *Magn Reson Med*, vol. 65, pp. 480–491, Feb. 2011.

[70] M. Akçakaya, S. Nam, P. Hu, M. H. Moghari, L. H. Ngo, V. Tarokh, W. J. Manning, and R. Nezafat, "Compressed sensing with wavelet domain dependencies for coronary MRI: a retrospective study.," *IEEE Trans Med Imaging*, vol. 30, pp. 1090–1099, May 2011.

[71] C. M. van Bemmel, L. J. Spreeuwers, M. A. Viergever, and W. J. Niessen, "Level-set-based artery-vein separation in blood pool agent CE-MR angiograms.," *IEEE Trans Med Imaging*, vol. 22, pp. 1224–1234, Oct. 2003.

[72] T. Lei, J. K. Udupa, P. K. Saha, and D. Odhner, "Artery-vein separation via MRA–an image processing approach.," *IEEE Trans Med Imaging*, vol. 20, pp. 689–703, Aug. 2001.

[73] K. Scheffler and S. Lehnhardt, "Principles and applications of balanced SSFP techniques," *Eur Radiol*, vol. 13, no. 11, pp. 2409–2418, 2003.

[74] D. C. Peters, D. B. Ennis, and E. R. McVeigh, "High-resolution MRI of cardiac function with projection reconstruction and steady-state free precession," *Magn Reson Med*, vol. 48, no. 1, pp. 82–88, 2002.

[75] O. Bieri, S. Patil, H. H. Quick, and K. Scheffler, "Morphing steady-state free precession," *Magn Reson Med*, vol. 58, pp. 1242–1248, 2007.

[76] I. Koktzoglou, D. Li, and R. Dharmakumar, "Dephased FLAPS for improved visualization of susceptibility-shifted passive devices for real-time interventional MRI," *Phys Med Biol*, vol. 52, no. 1, pp. 277–286, 2007.

[77] K. Scheffler, E. Seifritz, D. Bilecen, R. Venkatesan, J. Hennig, M. Deimling, and E. M. Haacke, "Detection of BOLD changes by means of a frequency-sensitive trueFISP technique: preliminary results," *NMR Biomed*, vol. 14, no. 7-8, pp. 490–496, 2001.

[78] K. L. Miller, B. A. Hargreaves, J. Lee, D. Ress, R. C. de Charms, and J. M. Pauly, "Functional brain imaging using a blood oxygenation sensitive steady-state," *Magn Reson Med*, vol. 50, no. 4, pp. 675–683, 2003.

[79] C. Heyn, C. V. Bowen, B. K. Rutt, and P. J. Foster, "Detection threshold of single SPIO-labeled cells with FIESTA," *Magn Reson Med*, vol. 53, pp. 312–320, 2005.

[80] K. S. Nayak, H.-L. Lee, B. A. Hargreaves, and B. S. Hu, "Wideband SSFP: Alternating repetition time balanced steady state free precession with increased band spacing," *Magn Reson Med*, vol. 58, no. 1, pp. 931–938, 2007.

[81] B. A. Hargreaves, "Partially dephased SSFP for elimination of dark bands," in *Proceedings of the 16th Annual Meeting of ISMRM*, (Toronto), p. 1357, 2008.

[82] T. Benkert, P. Ehses, M. Blaimer, P. M. Jakob, and F. A. Breuer, "Dynamically phase-cycled radial balanced SSFP imaging for efficient banding removal.," *Magn Reson Med*, vol. 73, pp. 182–194, Jan. 2015.

[83] H. Sun, J. A. Fessler, D. C. Noll, and J.-F. Nielsen, "Balanced SSFP-like steady-state imaging using small-tip fast recovery with a spectral prewinding pulse.," *Magn Reson Med*, vol. 75, pp. 839–844, Feb. 2016.

[84] J. Lee, M. Lustig, D. H. Kim, and J. M. Pauly, "Improved shim method based on the minimization of the maximum off-resonance frequency for balanced steady-state free precession (bSSFP).," *Magn Reson Med*, vol. 61, pp. 1500–1506, June 2009.

[85] Q.-S. Xiang and M. N. Hoff, "Banding artifact removal for bSSFP imaging with an elliptical signal model.," *Magn Reson Med*, vol. 71, pp. 927–933, Mar. 2014.

[86] M. Björk, R. R. Ingle, E. Gudmundson, P. Stoica, D. G. Nishimura, and J. K. Barral, "Parameter estimation approach to banding artifact reduction in balanced steady-state free precession.," *Magn Reson Med*, vol. 72, pp. 880–892, Sept. 2014.

[87] E. M. Haacke, P. A. Wielopolski, J. A. Tkach, and M. T. Modic, "Steady-state free precession imaging in the presence of motion: Application for improved visualization of the cerebrospinal fluid," *Radiology*, vol. 175, pp. 545–552, 1990.

[88] N. K. Bangerter, B. A. Hargreaves, S. S. Vasanawala, J. M. Pauly, G. E. Gold, and D. G. Nishimura, "Analysis of multiple-acquisition SSFP," *Magn Reson Med*, vol. 51, no. 5, pp. 1038–1047, 2004.

[89] A. M. Elliott, M. A. Bernstein, H. A. Ward, J. Lane, and R. J. Witte, "Nonlinear averaging reconstruction method for phase-cycle SSFP," *Magn Reson Imaging*, vol. 25, pp. 359–364, 2007.

[90] B. Quist, B. A. Hargreaves, T. Çukur, G. R. Morrell, G. E. Gold, and N. K. Bangerter, "Simultaneous fat suppression and band reduction with large-angle multiple-acquisition balanced steady-state free precession.," *Magn Reson Med*, vol. 67, pp. 1004–1012, Apr. 2012.

[91] B. Quist, B. A. Hargreaves, B. L. Daniel, and M. Saranathan, "Balanced SSFP Dixon imaging with banding-artifact reduction at 3 Tesla.," *Magn Reson Med*, vol. 74, pp. 706–715, Sept. 2015.

[92] Y. Wang, X. Shao, T. Martin, S. Moeller, E. Yacoub, and D. J. J. Wang, "Phase-cycled simultaneous multislice balanced SSFP imaging with CAIPIRINHA for efficient banding reduction; doi:10.1002/mrm.26076.," *Magn Reson Med*, vol. 0, no. 0, pp. 0–0, 2015.

[93] M. Lustig and J. M. Pauly, "SPIRiT: Iterative self-consistent parallel imaging reconstruction from arbitrary k-space.," *Magn Reson Med*, vol. 64, pp. 457–471, Aug. 2010.

[94] K. P. Pruessmann, M. Weiger, M. B. Scheidegger, and P. Boesiger, "SENSE: Sensitivity encoding for fast MRI," *Magn Reson Med*, vol. 42, no. 5, pp. 952–962, 1999.

[95] T. Çukur, M. Lustig, and D. G. Nishimura, "Multiple–profile homogenous image combination: Application to phase-cycled SSFP and multi-coil imaging," *Magn Reson Med*, vol. 60, pp. 732–738, 2008.

[96] M. Lustig, J. M. Santos, and J. M. Pauly, "A super-FOV method for rapid SSFP banding artifact reduction," in *Proceedings of the 13th Annual Meeting of ISMRM*, (Miami Beach), p. 504, 2005.

[97] M. L. Lauzon and R. Frayne, "Analytical characterization of RF phase-cycled balanced steady-state free precession," *Concepts Magn. Reson.*, vol. 34A, no. 3, pp. 133–143, 2009.

[98] L. Ying and J. Sheng, "Joint image reconstruction and sensitivity estimation in SENSE (JSENSE).," *Magn Reson Med*, vol. 57, pp. 1196–1202, June 2007.

[99] M. Uecker, T. Hohage, K. T. Block, and J. Frahm, "Image reconstruction by regularized nonlinear inversion–joint estimation of coil sensitivities and image content.," *Magn Reson Med*, vol. 60, pp. 674–682, Sept. 2008.

[100] M. Doneva, P. Börnert, H. Eggers, C. Stehning, J. Sénégas, and A. Mertins, "Compressed sensing reconstruction for magnetic resonance parameter mapping.," *Magn Reson Med*, vol. 64, pp. 1114–1120, Oct. 2010.

[101] D. L. Donoho and J. M. Johnstone, "Ideal spatial adaptation by wavelet shrinkage," *Biometrika*, vol. 81, no. 3, pp. 425–455, 1994.

[102] D. F. Yu and J. A. Fessler, "Edge-preserving tomographic reconstruction with nonlocal regularization.," *IEEE Trans Med Imaging*, vol. 21, pp. 159–173, Feb. 2002.

[103] A. Chambolle, "Total Variation Minimization and a Class of Binary MRF Models," in *Lecture Notes in Computer Science* (A. Rangarajan, B. Vemuri, and A. Yuille, eds.), pp. 136–152–152, Berlin, Heidelberg: Springer Berlin Heidelberg, 2005.

[104] M. Uecker, P. Lai, M. J. Murphy, P. Virtue, M. Elad, J. M. Pauly, S. S. Vasanawala, and M. Lustig, "ESPIRiT–an eigenvalue approach to autocalibrating parallel MRI: where SENSE meets GRAPPA.," *Magn Reson Med*, vol. 71, pp. 990–1001, Mar. 2014.

[105] F. Huang, Y. Chen, W. Yin, W. Lin, X. Ye, W. Guo, and A. Reykowski, "A rapid and robust numerical algorithm for sensitivity encoding with sparsity constraints: self-feeding sparse SENSE.," *Magn Reson Med*, vol. 64, pp. 1078–1088, Oct. 2010.

[106] T. Cukur, J. M. Santos, D. G. Nishimura, and J. M. Pauly, "Varying kernel-extent gridding reconstruction for undersampled variable-density spirals.," *Magn Reson Med*, vol. 59, pp. 196–201, Jan. 2008.

[107] T. Çukur, J. M. Santos, J. M. Pauly, and D. G. Nishimura, "Variable-density parallel imaging with partially localized coil sensitivities.," *IEEE Trans Med Imaging*, vol. 29, pp. 1173–1181, May 2010.

[108] S. Boyd, N. Parikh, E. Chu, B. Peleato, and J. Eckstein, "Distributed Optimization and Statistical Learning via the Alternating Direction Method of Multipliers," *Found. Trends Mach. Learn.*, vol. 3, no. 1, pp. 1–122, 2011.

[109] K. S. Nayak, B. A. Hargreaves, B. S. Hu, D. G. Nishimura, J. M. Pauly, and C. H. Meyer, "Spiral balanced SSFP cardiac imaging," *Magn Reson Med*, vol. 53, no. 1, pp. 1468–1473, 2005.

[110] T. Çukur and D. G. Nishimura, "Fat-water separation with alternating repetition time balanced SSFP," *Magn Reson Med*, vol. 60, pp. 479–484, 2008.

[111] T. Akasaka, K. Fujimoto, T. Yamamoto, T. Okada, Y. Fushumi, A. Yamamoto, T. Tanaka, and K. Togashi, "Optimization of regularization parameters in compressed sensing of magnetic resonance angiography: Can statistical image metrics mimic radiologists' perception?," *PLOS ONE*, vol. 11, pp. 1–14, 01 2016.

[112] K. Khare, C. J. Hardy, K. F. King, P. A. Turski, and L. Marinelli, "Accelerated mr imaging using compressive sensing with no free parameters," *Magnetic Resonance in Medicine*, vol. 68, no. 5, pp. 1450–1457, 2012.

[113] S. Ramani, D. S. Weller, J. F. Nielsen, and J. A. Fessler, "Non-cartesian mri reconstruction with automatic regularization via monte-carlo sure," *IEEE Transactions on Medical Imaging*, vol. 32, pp. 1411–1422, Aug 2013.

[114] D. S. Weller, S. Ramani, J. Nielsen, and J. A. Fessler, "Monte carlo SURE-based parameter selection for parallel magnetic resonance imaging reconstruction," *Magnet Reson Med*, vol. 71, no. 5, pp. 1760–1770, 2014.

[115] E. Ilicak and T. Çukur, "Parameter-free profile encoding reconstruction for multiple-acquisition bSSFP imaging," in *Proceedings of the 25th Annual Meeting of ISMRM*, (Honolulu), p. 571, 2017.

[116] C.-H. Chang, X. Yu, and J. X. Ji, "Compressed sensing mri reconstruction from 3d multichannel data using gpus," *Magnetic Resonance in Medicine*, 2017.

[117] T. A. Basha, M. Akçakaya, C. Liew, C. W. Tsao, F. N. Delling, G. Addae, L. Ngo, W. J. Manning, and R. Nezafat, "Clinical performance of high-resolution late gadolinium enhancement imaging with compressed sensing," 2017.